CHALMERS
UNIVERSITY OF TECHNOLOGY

Motion prediction of a heavy vehicle to avoid understeer and rollover

Modelling and simulations of a heavy rigid truck with motion prediction and control envelope to maintain safe driving conditions

Master's thesis in Systems, Control and Mechatronics

CECILIA BUSTRÉN

DEPARTMENT OF MECHANICS AND MARITIME SCIENCES
CHALMERS UNIVERSITY OF TECHNOLOGY
Gothenburg, Sweden 2022
www.chalmers.se

Master's thesis 2022

Motion prediction of a heavy vehicle to avoid understeer and rollover

Modelling and simulation of a heavy rigid truck with motion prediction and control envelope to maintain safe driving conditions

CECILIA BUSTRÉN

CHALMERS
UNIVERSITY OF TECHNOLOGY

Department of Mechanics and Maritime Sciences
Division of Vehicle Engineering and Autonomous Systems
Chalmers University of Technology
Gothenburg, Sweden 2022

Motion prediction of a heavy vehicle to avoid understeer and rollover
Modelling and simulation of a heavy rigid truck with motion prediction and control envelope to maintain safe driving conditions
CECILIA BUSTRÉN

Supervisor: Leo Laine, Volvo GTT
Examiner: Mats Jonasson, Department of Mechanics and Maritime Sciences, Chalmers University of Technology

Master's Thesis 2022:64
Department of Mechanics and Maritime Sciences
Division of Vehicle Engineering and Autonomous Systems
Chalmers University of Technology
SE-412 96 Gothenburg
Telephone +46 31 772 1000

Cover: Volvo electric rigid truck.

Typeset in LaTeX
Printed by Chalmers Reproservice
Gothenburg, Sweden 2022

Motion prediction of a heavy vehicle to avoid understeer and rollover
Modelling and simulation of a heavy rigid truck with motion prediction and control envelope to maintain safe driving conditions
CECILIA BUSTRÉN
Department of Mechanics and Maritime Sciences
Chalmers University of Technology

Abstract

This thesis concerns an investigation of a safety system to avoid rollover and understeering in a heavy vehicle. This safety system includes a motion prediction with implemented braking action, as well as a yaw controller. The motion prediction has a 2 second prediction horizon, and the braking action is implemented in all wheels. The motion prediction includes a model of the vehicle based on Newtonian formalism and the tire model is based on the Pacejka 2002 model. The yaw controller is a QFT design, and is implemented on the rear wheels.

The contribution to the field is the investigation of a real-time motion prediction safety system, which aims to reduce the risk of rollover and understeering under normal driving conditions. The objective is that this system would predict and implement a preventive action sooner than a driver realistically could, thus reducing the risk of a critical traffic situation.

The thesis work has been conducted through computations and simulations in Matlab and Simulink, and simulations in C++.

Acknowledgements

Firstly I would like to thank my supervisor Dr. Leo Laine for the opportunity to conduct my thesis work at Volvo Group Truck Technology, and for his unique insight to the field and very helpful guidance throughout the process.

I am very grateful to Niklas Fröjd at Volvo Group Truck Technology for his expert help on tire modelling, and his patience for my many questions.

I would also like to thank my examiner Mats Jonasson at Chalmers University of Technology for his feedback and guidance throughout the thesis process.

Last but not least, a special thanks to my friend and colleague Salmane Essayeh for his cooperation and support during our respective theses. You have been a great help and your remarkable skills in programming and vehicle dynamics have been instrumental in the success of my thesis.

Cecilia Bustrén, Gothenburg, June 2022

Nomenclature

Below is the nomenclature of indices, sets, parameters, and variables that have been used throughout this thesis.

Indices

i	Index for vehicle unit
j	Index for unit axle

Parameters

L	Length from centre of gravity to axle	m
l	Length from centre of axle to wheel	m
m	Unit mass	kg
I_{zz}	Vertical inertial force at centre of gravity	$kg\,m^2$
A_f	Longitudinally projected area in the direction of motion	m^2
C_{ae}	Aerodynamic drag coefficient	
C_{rr}	Rolling resistance coefficient	
g	Standard gravity	$g = 9.81$

Variables

δ	Steering wheel angle	rad
β	Road slope	rad
ψ	Yaw angle at centre of gravity	rad
$\dot{\psi}$	Yaw rate at centre of gravity	$rad\,s^{-1}$
$\ddot{\psi}$	Angular/yaw acceleration at centre of gravity	$rad\,s^{-2}$
$\Delta\psi$	Articulation angle	rad
$\mathbf{v}$	Velocity at centre of gravity	$m\,s^{-1}$

$\mathbf{F}$	Force at centre of gravity	N
$\mathbf{F}_w$	Tire force	N
F_a	Aerodynamic drag force	N
F_{rr}	Rolling resistance force	N
F_s	Slope resistance force	N
Γ_y	Vehicle lateral force	g
$\mathbf{a}$	Acceleration at centre of gravity	$m\,s^{-2}$
$\mathbf{M}$	Moment at centre of gravity	Nm
μ	Road friction coefficient	
κ	Longitudinal tire slip	
α	Lateral tire slip angle	rad or $^\circ$
K_{us}	Understeering gradient	$rad\,s^2\,m^{-1}$

Contents

List of Figures

List of Tables

1

Introduction

1.1 Background

Due to the significant weight and size of trucks, accidents on the road concerning trucks are potentially very serious. Most common accidents involving trucks are between trucks and passenger cars. Severe situations causing a loss of control, such as rollover or jack knife, most often occur when cornering at excessive speed [24]. To reduce the risk of traffic accidents, various motion support and stability control systems are developed and implemented as vehicle stability control systems with the primary function of maintaining control over the vehicle in the case of potentially severe situations [8][22].

Some stability control systems currently in use include Roll Stability Control (RSC), Electronic Stability Control (ESC) and Anti-lock Breaking Systems (ABS), among others [1]. These systems continuously monitor a series of motion indicators from on-board sensors and make a prediction of future vehicle motion. If the system predicts a loss of control or traction, some automatic change of motion is applied, such as a reduction of the speed or an implementation of a corrective steering moment. Studies have shown that active safety systems such as these can significantly reduce the risk of severe situations such as jack knife, under- or oversteering, especially in emergency steering manoeuvres or unfavourable road conditions. In this thesis, a new motion prediction function with implemented braking action is investigated for avoiding understeer and rollover.

There are a number of limits to stability control systems. They cannot always be sufficient to prevent loss of control in every type of situation, especially when the vehicle is at an excessive speed. In these situations an incident such as rollover may not be preventable, even if the stability control system is engaged. The system may, however, still be able to reduce the severity of the occurrence by, for example, reducing the speed. In cases of vehicle failures, such as the loss or puncture of a wheel, the stability control systems are not able to effectively engage in maintaining control of the vehicle [8].

1.2 Objective

The purpose of this thesis is to develop and evaluate a motion prediction and control model for a rigid truck in order to prevent two critical situations under normal driving conditions, namely rollover and understeering. The goal is that this model could be implemented in real time, and as such needs to be sufficiently accurate and run in a sufficiently fast computation time in order to be effective. The model will consider two input signals from the driver: acceleration from the pedals, $a_{x,driver}$, and steering angle, δ. Road friction, μ, will also be given as inputs. Other environmental inputs such as wind, road inclination angle or the presence of other vehicles are not considered in this thesis. A successful motion prediction controller will be able to predict and implement preventative action more rapidly than a driver, with limited reflexes, would be able to, thus reducing the risk of traffic accidents.

Proper motion predictions are necessary to perform to assure safe transports with commercial heavy vehicle combinations with high productivity. The vehicle motion management (VMM) needs to do motion estimation, motion prediction and motion coordination of the Motion Support Devices (MSD). This thesis is limited to only deal with motion prediction.

There are generally three types of motion model classifications [17] used for prediction. The simplest type is physics-based motion models, which consider that the motion of the vehicle depends only on the laws of physics. The second is manoeuvre-based motion models, which also considers that the future motion of the vehicle depends on the manoeuvre input from the driver. The third and most advanced type is interaction-aware motion models, which take into account the inter-dependencies between other vehicles and the environment. In this thesis we will be working with a manoeuvre-based model, i.e. we will have a model with driver input, however we will not take other vehicles or environmental input into account. The driver inputs are steering angle δ and pedal action a_x.

In motion prediction, the future motion is predicted within a prediction horizon using current automated or manual driver inputs. These inputs can either be predicted to change or be kept constant during the predictions. The length of the prediction horizon will have to take into account the 0.5 s delay between submitting a control action, such as breaking, and the action being carried out by the actuators. Prediction and control is conducted to avoid reaching the control envelope. This to avoid rollover and understeering. If the motion prediction is foreseeing a rollover or understeer situation in the next prediction horizon, the vehicle longitudinal velocity ($v_{x,max}$) capability and acceleration capability ($a_{x,max}$) to the Traffic Situation Management (TSM) is limited before the event occurs. Along with the motion, the uncertainty (e.g. covariance) associated with the prediction is also estimated. This takes into account the uncertainties in the vehicle model, the driver inputs and also the motion estimation at the current instant which serves as the starting point for the prediction.

Some assumptions of the vehicle are made, in order to simplify the thesis. The mass of the truck is assumed to be uniformly distributed from the centre of gravity. The tire parameters are assumed to be known, as well as the road friction and road slope.

2

Critical Situations Definitions

This chapter defines the critical situations which are discussed in this thesis. The aim of the prediction and control model is to avoid these situations under normal driving conditions.

2.1 Understeering

Understeering occurs when the tire slip of the front tires exceed that of the rear tires, i.e. the vehicle is not turning sufficiently to match the steering angle of the tires. The front wheels of the vehicle lose traction and their steering angle exceeds that of the vehicle's, $\delta_{steering} > \delta_{vehicle}$. This mainly occurs at low road friction levels, however it can occur at all friction levels under certain circumstances.

Understeering occurs when there is insufficient lateral force available to the vehicles front tires. This is mainly the reason to why understeering is most prominent at low road friction levels, since we have a more limited amount of lateral tire force at our disposal then. Thus, to avoid understeering, we must secure sufficient lateral tire force. However, since we cannot increase the amount of force that can physically be available, we have to ensure that the vehicle does not enter into situations which require lateral force that exceeds the physical limit. Understeering may be reduced or avoided by implementing yaw control and wheel torque allocation techniques, such as an electronic brake control (EBS). Another way to reduce or avoid understeering is to limit the velocity of the vehicle to match the road friction level.

One way to measure the degree of understeering in a vehicle is by the understeering gradient, K_{us}, which is calculated from the steering angle δ, the length between the front and rear axles L, the yaw rate ψ, the longitudinal velocity v_x and the lateral acceleration a_y.

$$K_{us} = \frac{\delta - \frac{L\psi}{v_x}}{a_y} \tag{2.1}$$

Understeering is present when the understeering gradient K_{us} is greater than 0.

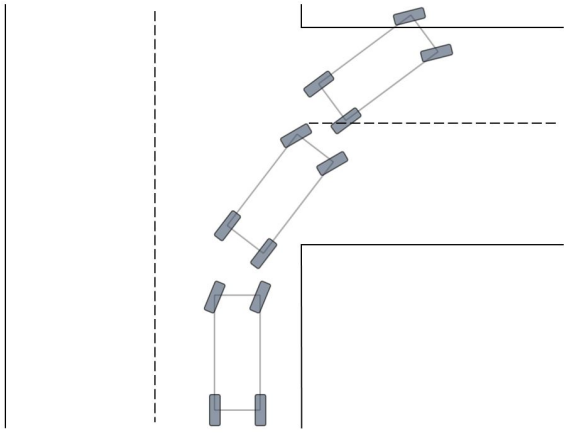

Figure 2.1: Depiction of understeering in road turn.

2.2 Oversteering

Oversteering correspondingly occurs when the tire slip of the rear tires exceeds that of the front tires, i.e. the rear wheels lose traction and the vehicle turns with a greater angle than the tire steering angle, $\delta_{vehicle} > \delta_{steering}$. Generally, oversteering most often occurs in combination with understeering in e.g. swerving scenarios.

Analogously to understeering, oversteering occurs when there is insufficient lateral tire force of the rear tires. As with understeering, one way to avoid or decrease oversteering is to implement yaw control and torque allocation techniques. Another is to limit the vehicles velocity in correspondence to the road friction level.

Oversteering is present when the understeering gradient K_{us} is negative.

2.3 Rollover

Rollover occurs due to excessive lateral (centrifugal) force of a vehicle, and is induced when the vehicle attempts a tight curve at an exceedingly high velocity. A vehicles lateral acceleration cannot physically exceed μg, where μ is the road friction level and g is the standard gravity. Therefore rollover will only occur at road surfaces that exceed approximately $\mu = 0.35$, since the lateral acceleration limit for rollover is approximately $\Gamma_y = 0.35g$.

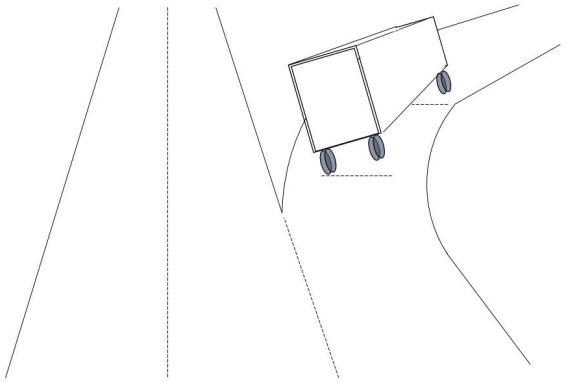

Figure 2.2: Depiction of rollover in road turn.

The lateral acceleration is in this thesis denoted as Γ_y and is computed from Newtons second law of motion, where F_y denotes lateral force and m denotes mass.

$$\Gamma_y = \frac{\sum F_y}{m} \tag{2.2}$$

Although rollover may begin at either axle, it most commonly begins at the rear of the vehicle, thus the inner rear tire is generally the first to lift off the ground. For combination vehicles there is also often a rearward amplification induced, where the consecutive units will have an amplification in lateral acceleration as compared to the former unit. This amplification can be calculated and depends on the placement of the coupling between the units. Since this thesis concerns a rigid truck, rearward amplification is not discussed further in the report.

The risk of rollover is highly dependent on environmental factors, such as road conditions and wind conditions. Studies have shown that the risk of rollover increased threefold when doubling the subjected wind speeds from 20 mph (approximately 9 m/s) to 40 mph (approximately (18 m/s) [2]. The direction of the wind force to the truck also significantly influences the risk of rollover. This thesis will however not consider wind as a factor. Rollover risk is also dependent on load distribution, however this is considered uniform from the centre of gravity in this thesis.

3

Vehicle Modelling

A motion model of the vehicle was derived for the motion prediction implementation this thesis. The model needs to satisfy two conditions: it needs to be sufficiently accurate in order to realistically describe the truck in motion, and also be sufficiently simple for the computations to be able to run in real time. In order to deal with this trade-off in accuracy versus computation time, the most simple model possible was initially implemented, and adaptions were made along the study where adaptions and improvements were deemed most necessary. The initial model was a simple one-track model, which was eventually adapted into a more comprehensive 4-wheel model, which allows for individual brake allocation at each wheel. The model was derived using Newton formalism.

Newton formalism is based on Newton's laws of motion, and calculates the vehicle's motion based on the forces present. It is a simple and straightforward approach of modelling and is a natural choice of formalism when considering a classic mechanical phenomena. Lagrangian formalism derives the vehicle's motion by considering energies, and is based on the principle of least action. This principle considers every path a an object can take through time and space and minimises a quantity referred to as an action associated with this path. The Lagrangian formalism is in this way preferable to Newtonian formalism when considering cases that stretch beyond classical mechanics, such as relativity physics or quantum theories.

The disadvantage of using Newton formalism is that the computation of the coupling forces between two vehicle units is considerably more complicated, and the number of equations necessary to represent these are therefore greater. For the Newtonian approach, the coupling forces must be explicitly known and included in the the model in order to solve the equations of motion. The equations of motion can be solved without calculating the coupling constraints when using Lagrange formalism, which makes this method superior when dealing with complicated constraints.

This section includes a kinetic one-track model which is general to any vehicle combination [5][4]. The modelling of a 4x2 rigid truck is then presented, which is adapted from the one-track model [25][3]. Modelling of a tractor and semitrailer combination vehicle was also derived, in both Newton- and Lagrange formalism, however the results for this is not presented in the thesis. The semitrailer combination models can be found in Appendix A.

3.1 Kinetic One-Track Model

The equations of motion are derived using Newton formalism. Newton's second law of motion is applied to each vehicle unit. The centre of gravity is considered as constant throughout the motion for each unit and the mass of each unit is distributed uniformly from the centre of gravity. Newton's third law of motion is applied to the coupling forces between units, i.e. the forces applied from the coupling point to each unit is equal and opposite when considered in the same frame of space. Kinematic equations are considered between the vehicle units, and aerodynamic drag is neglected for all sides of the vehicle except for the front, ergo this friction is simplified and only considered for the first unit. Tire forces are computed using the Pacejka model and the method for this is described in Section 4.1.

The total sum of forces acting on a vehicle unit is defined from Newton's second law.

$$\sum \mathbf{F}_i = m_i \cdot \mathbf{a}_i \tag{3.1}$$

The acceleration at the centre of gravity is calculated from the velocity at the centre of gravity, $\mathbf{v}_i = [v_{x,i}, v_{y,i}, 0]^T$, and the angular velocity at the centre of gravity, $\dot{\Psi}_i = [0, 0, \dot{\psi}_i]^T$.

$$\mathbf{a}_i = \dot{\mathbf{v}}_i + \dot{\Psi}_i \times \mathbf{v}_i$$

From Newton's laws we also get a relationship between the unit moment, vertical inertial force and angular acceleration at the centre of gravity.

$$\sum \mathbf{M}_i = I_{zz,i} \cdot \ddot{\Psi}_i \tag{3.2}$$

The unit moment is comprised of tire moments and coupling moments, around the centre of mass. These are calculated from the tire or coupling force and the position vector from the centre of gravity to the tire or coupling point. The vertical difference is neglected in this model and these distance vectors are given as $\mathbf{r}_{ij} = [L_{ij}, l_{ij}, 0]^T$ from centre of gravity to tire and $\mathbf{r}_{c,ip} = [L_{c,ip}, 0, 0]^T$ from centre of gravity to coupling point, where i is the vehicle unit, j is the axle, $n = R, L$ is the right or left side tire and $p = 1, 2$ is the front and rear coupling.

$$\begin{aligned} \mathbf{M}_{ijn} &= \mathbf{r}_{ij} \times \mathbf{F}_{ijn} \\ \mathbf{M}_{ip} &= \mathbf{r}_{cip} \times \mathbf{F}_{cip} \end{aligned} \tag{3.3}$$

Equations 3.3 are valid for tire forces $\mathbf{F}_{ijn} = [F_{x,ijn}, F_{y,ijn}, 0]^T$ and coupling forces $\mathbf{F}_{cip} = [F_{cx,ip}, F_{cy,ip}, 0]^T$ in unit frame.

Articulation angle, $\Delta\psi$, between two coupled units is defined as the difference in their respective yaw angles, ψ.

$$\Delta\psi_i = \psi_i - \psi_{i+1} \tag{3.4}$$

The aerodynamic drag force acting on the vehicle is calculated from the air density ρ, the longitudinally projected area in the direction of motion A_f, the drag coefficient C_{ae} and the longitudinal velocity of the vehicle v_x.

$$F_a = \frac{1}{2} \rho \, A_f \, C_{ae} \, v_x^2 \, \text{sign}(v_x) \tag{3.5}$$

Disturbance force from wind and weather will not be included in the model. i.e. the aerodynamic force is assumed only to be acting on the frontal area of the truck.

The rolling resistance is calculated from the unit mass m, the rolling resistance coefficient C_{rr} and the longitudinal velocity of the vehicle v_x, as derived in [16].

$$F_{rr} = m\, C_{rr}\, (1 - e^{-\frac{1}{2}|v_x|})\, \text{sign}(v_x) \tag{3.6}$$

The slope resistance force is calculated from the mass m, the standard gravity $g = 9.81$ and the road slope β.

$$F_s = m\, g\, \sin(\beta) \tag{3.7}$$

3.1.1 4 Wheel Model of a Rigid Truck

This thesis concerns a rigid 4x2 truck. Since this truck has only one unit, it is relatively straightforward to model this vehicle using Newton formalism. A vector representation of the spacial and kinematic parameters are presented in Figure 3.1.

The model is a 4 wheel model rather than a bicycle model in order to estimate a virtual torque used for yaw control.

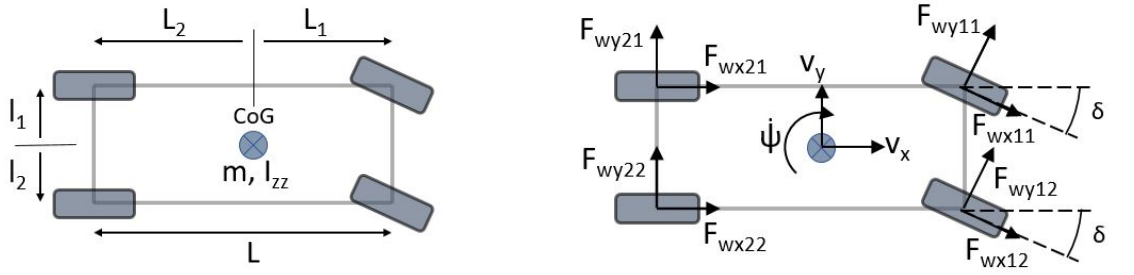

(a) Spacial parameters of a 4x2 rigid truck.

(b) Dynamic parameters of a 4x2 rigid truck.

Figure 3.1: Schematic depiction of parameters of a 4x2 rigid truck.

The tire forces acting on the vehicle are modelled in Section 4.1 and are calculated in the wheel frame. The tire forces are translated into vehicle frame using a rotation matrix. The notation $j = \{1, 2\}$ specifies the axle and the notation $n = \{1, 2\}$ specifies the left or right tire on the axle.

$$\begin{bmatrix} F_{x,jn} \\ F_{y,jn} \end{bmatrix} = \begin{bmatrix} \cos\delta & -\sin\delta \\ \sin\delta & \cos\delta \end{bmatrix} \begin{bmatrix} F_{wx,jn} \\ F_{wy,jn} \end{bmatrix} \tag{3.8}$$

From Newton's second law, Equations 3.1-3.7, we get the equations of motion for this vehicle. Aerodynamic drag, rolling resistance and slope resistance force are included in the longitudinal dynamics, however any resistance forces are in the lateral dynamics are assumed negligible. Drag force from wind is excluded in the

model due to the complexity of determining relative wind speeds during motion. The equations of motion are expressed in vehicle frame in Equations 3.9-3.10 and expressed with wheel forces given in wheel frame in Equations 3.11-3.12.

$$m(\dot{v}_x - \dot{\psi}\, v_y) = F_{x,11} + F_{x,12} + F_{x,21} + F_{x,22} - F_a - F_{rr} - F_s \tag{3.9}$$

$$m(\dot{v}_y + \dot{\psi}\, v_x) = F_{y,11} + F_{y,12} + F_{y,21} + F_{y,22} \tag{3.10}$$

$$\begin{aligned} m(\dot{v}_x - \dot{\psi}\, v_y) = &(F_{wx11} + F_{wx12})\cos\delta - (F_{wy11} + F_{wy12})\sin\delta \\ &+ F_{wx21} + F_{wx22} - F_a - F_{rr} - F_s \end{aligned} \tag{3.11}$$

$$\begin{aligned} m(\dot{v}_y + \dot{\psi}\, v_x) = &(F_{wx11} + F_{wx12})\sin\delta + (F_{wy11} + F_{xy12})\cos\delta \\ &+ F_{wy21} + F_{xy22} \end{aligned} \tag{3.12}$$

The torque applied to the vehicle units are calculated in vehicle frame according to 3.2 and 3.3.

$$I_{zz}\ddot{\psi} = (F_{y11} + F_{y12})\, L_1 + (F_{y21} + F_{y22})\, L_2 - (F_{x11} + F_{x12})\, l_1 - (F_{x21} + F_{x22})\, l_2 \tag{3.13}$$

The 4-wheel model allows for a virtual torque to be introduced, which can then be used for yaw control of the vehicle in motion. The virtual torque, T_v, is defined as the torque quota offered from the partition of the vehicle's rear wheels. The virtual torque is introduced from Equation 3.13 as expressed with wheel forces in wheel frame.

$$\begin{aligned} I_{zz}\ddot{\psi} = &[(F_{wx11} + F_{wx12})\sin\delta + (F_{wy11} + F_{xy12})\cos\delta]\, L_1 \\ &+ [(F_{wx12} - F_{wx11})\cos\delta + (F_{wy11} - F_{wy12})\sin\delta]\, l_1 \\ &- [F_{wy22} + F_{xy21}]\, L_2 + [F_{wx22} - F_{xx21}]\, l_2 \\ = &[(F_{wx11} + F_{wx12})\sin\delta + (F_{wy11} + F_{xy12})\cos\delta]\, L_1 \\ &+ [(F_{wx12} - F_{wx11})\cos\delta + (F_{wy11} - F_{wy12})\sin\delta]\, l_1 \\ &- [F_{wy22} + F_{xy21}]\, L_2 + T_v \end{aligned} \tag{3.14}$$

The virtual torque can then be expressed in terms of the longitudinal tire slip κ and the longitudinal slip stiffness K_x, as introduced in Chapter 4.1.

$$\begin{aligned} T_v &= l_2\,(F_{wx22} - F_{wx21}) \\ &= l_2\, K_{x2}\,(\kappa_2^E + \kappa_{22}(t) - \kappa_2^E - \kappa_{21}(t)) \end{aligned} \tag{3.15}$$

The virtual torque is used for yaw control by differential slip ratio, as presented in Section 5.1.

The lateral force of the vehicle, here denoted Γ_y, is calculated for roll-over control.

$$\Gamma_y = \sum F_{y1i} \tag{3.16}$$

The individual lateral force of the front and rear axles are calculated for roll-over control at each axle. Note that the length to the front axle is positive and the length to the rear axle is negative.

$$\Gamma_{y,i} = \Gamma_y + \psi_1^2 * L_i \tag{3.17}$$

4

Tire Modelling

There are several established methods of modelling the tire forces of a vehicle. Several tire models have been considered for this thesis, among these the Pacejka 1994 model [21], the Pacjeka 2002 [15] (PAC2002) model and the Brush model have been investigated further. The PAC2002 model is implemented in this thesis and presented in this section, with some simplifications. The full PAC2002 model, an adaption of the PAC2002 model and the Brush model are presented in Appendix B.

4.1 Pacejka Tire Models

The Pacejka models are centred around longitudinal tire slip κ and lateral tire slip angle α. A well established central formula called the "Magic Formula" serves as a basis for all models, as well as a number of tire specific coefficients which are determined by the tire's individual characteristics. The magic formula is an empirical formula and is considered to work well for all road slip quantities, as well as for combined slip.

4.1.1 Definitions of Tire Slip Quantities

The effective rolling radius r_0 is obtained by dividing the longitudinal velocity of a wheel, v_x, by the angular speed of revolution, Ω_0.

$$r_0 = \frac{v_x}{\Omega_0} \tag{4.1}$$

From this, the longitudinal tire slip κ may be obtained.

$$\kappa = \frac{r_0\Omega - v_x}{r_0\Omega} \tag{4.2}$$

For a free rolling vehicle, the longitudinal tire slip is, at least in theory, null. When a torque is applied to the wheel, we get either a positive or negative tire slip, depending on if the torque is applied for acceleration or breaking.

$$\text{if:} \quad r_0\Omega(t) - v_x(t) \geq 0 \quad \longrightarrow \quad \kappa = \frac{r_0\Omega - v_x}{r_0\Omega} \geq 0 \tag{4.3}$$

$$\text{if:} \quad r_0\Omega(t) - v_x(t) < 0 \quad \longrightarrow \quad \kappa = \frac{r_0\Omega - v_x}{v_x} < 0 \tag{4.4}$$

It follows from this that a driving axle may take tire slip values $\kappa \in \{-1, 1\}$, however a non-driving axle may only take tire slip values $\kappa \in \{-1, 0\}$.

The lateral wheel slip is defined as the ratio between the lateral and longitudinal velocities of a wheel. From this definition, we obtain the formulation of the lateral tire slip angle α, which is defined as minus the arcus tangent of the lateral wheel slip. The negative sign in the equation ensures that the lateral force and slip angle maintain the same sign.

$$\tan \alpha = -\frac{v_y}{|v_x|} \tag{4.5}$$

4.1.2 Magic Formula

The magic formula is a general semi-empirical model for steady-state longitudinal and lateral tire forces, which holds for given values of camber angle and vertical load.

$$y(x) = D \cos(C \arctan(Bx - E(Bx - \arctan(Bx)))) \tag{4.6}$$

$$Y(X) = y(x) + S_V \tag{4.7}$$

$$x = X + S_H \tag{4.8}$$

$Y(x)$ is either the longitudinal tire force F_x with $X = \kappa$ or it is the lateral tire force F_y with $X = \alpha$. The peak factor D determines the peak characteristic. The shape factor C determines the part used for sine, and therefore mainly influences the shape of the curve. The stiffness factor B stretches the curve. The curvature factor E modifies the characteristic around the peak of the curve. S_V is the vertical shift and S_H is the horizontal shift.

4.1.3 Modified PAC2002 Tire Model

The tire models presented below are adapted for the specific truck considered in this thesis, and as such the formulas presented have been modified from the original Pacejka formulas to exclude some parameters which are assumed zero, such as camber angle and some other tire specific parameters. The full PAC2002 model formulas are found in Appendix B.1.

The PAC2002 model is based on the Magic Formula. First, longitudinal and lateral forces for pure slip are computed. These are then multiplied by a weighting function, which accounts for the combined slip. The model uses normalised vertical load df_z as a measure for the vertical load.

$$df_z = \frac{F_z - F_{z0}}{F_{z0}} \tag{4.9}$$

The longitudinal force at pure slip, F_{x0}, is computed from the Magic Formula, and considers no lateral slip, $\alpha = 0$.

$$F_{x_0} = D_x \sin(C_x \arctan(B_x \kappa - E_x (B_x \kappa - \arctan(B_x \kappa)))) \tag{4.10}$$

The coefficients to F_{x0} are computed using some tire specific parameters and are dependent on vertical load and road friction. The values for these parameters are derived from physical tire testing.

$$
\begin{aligned}
B_x &= \frac{K_x}{C_x\, D_x} \\
C_x &= p_{Cx1} \\
D_x &= \mu_x\, F_z \\
E_x &= (p_{Ex1} + p_{Ex2}\, df_z + p_{Ex3}\, df_z^2) \\
K_x &= F_z\, (p_{Kx1} + p_{Kx2}\, df_z) \exp(p_{Kx3}\, df_z) \\
\mu_x &= (p_{Dx1} + p_{Dx2}\, df_z)\, \mu
\end{aligned}
$$

Table 4.1 provides brief explanations to the longitudinal pure slip coefficients.

Coefficient	Description
p_{Cx1}	Longitudinal force shape factor
p_{Dx1}	Longitudinal friction μ_x at $F_{z,nom}$
p_{Dx2}	Variation of friction μ_x with load
p_{Ex1}	Longitudinal curvature at $F_{z,nom}$
p_{Ex2}	Variation of curvature with load
p_{Ex3}	Variation of curvature with load squared
p_{Kx1}	Longitudinal slip stiffness at $F_{z,nom}$
p_{Kx2}	Variation of slip stiffness with load
p_{Kx3}	Exponent in slip stiffness with load

Table 4.1: Description of the longitudinal pure slip tire force coefficients.

The longitudinal weighting function $G_{x\alpha}$ accounts for combined slip in the longitudinal tire forces.

$$G_{x\alpha} = \cos(C_{x\alpha}\, \arctan(B_{x\alpha}\, \alpha - E_{x\alpha}\, (B_{x\alpha}\, \alpha - \arctan(B_{x\alpha}\, \alpha)))) \tag{4.11}$$

The coefficients to the weighting function are computed from tire specific parameters and are dependent on vertical load.

$$
\begin{aligned}
C_{x\alpha} &= r_{Cx1} \\
B_{x\alpha} &= r_{Bx1}\, \cos(\arctan(r_{Bx2}\, \kappa)) \\
E_{x\alpha} &= r_{Ex1} + r_{Ex2}\, df_z
\end{aligned}
$$

Table 4.2 provides brief explanations to the longitudinal combined slip coefficients.

Coefficient	Description
r_{Bx1}	Slope factor for combined slip longitudinal force reduction
r_{Bx2}	Variation of slope longitudinal force reduction with κ
r_{Cx1}	Shape factor for combined slip longitudinal force reduction
r_{Ex1}	Curvature factor of combined longitudinal force
r_{Ex2}	Curvature factor of combined longitudinal force with load

Table 4.2: Description of the longitudinal combined slip tire force coefficients.

The resultant longitudinal combined slip tire force F_x is given as the product of the pure slip tire force and weighting function.

$$F_x = F_{x0}\, G_{x\alpha}(\alpha,\, \kappa,\, F_z) \tag{4.12}$$

The lateral force at pure slip, F_{y0}, is computed from the Magic formula and considers no longitudinal slip, $\kappa = 0$.

$$F_{y0} = D_y\, \sin(C_y\, \arctan(B_y\, \alpha - E_y\, (B_y\, \alpha - \arctan(B_y\, \alpha)))) \tag{4.13}$$

The coefficients to the pure slip lateral force are computed from tire specific parameters and are dependent on vertical load and road friction.

$$\begin{aligned}
B_y &= \frac{K_y}{C_y\, D_y} \\
C_y &= p_{Cy1} \\
D_y &= \mu_y\, F_z \\
E_y &= (p_{Ey1} + p_{Ey2}\, df_z) \\
K_y &= p_{Ky1}\, F_{z_0}\, \sin(2\, \arctan(\frac{F_z}{p_{Ky2}\, F_{z_0}})) \\
\mu_y &= (p_{Dy1} + p_{Dy2}\, df_z)\, \mu
\end{aligned}$$

Table 4.3 provides brief explanations to the lateral pure slip coefficients.

Coefficient	**Description**
p_{Cy1}	Lateral force shape factor
p_{Dy1}	Lateral friction μ_y
p_{Dy2}	Variation of friction μ_y with load
p_{Ey1}	Lateral curvature at $F_{z,nom}$
p_{Ey2}	Variation of curvature with load
p_{Ky1}	Maximum lateral stiffness value
p_{Ky2}	Load at which maximum lateral stiffness is reached

Table 4.3: Description of the lateral pure slip tire force coefficients.

The lateral weighting function $G_{y\kappa}$ accounts for combined slip in the lateral tire forces.

$$G_{y\kappa} = \cos(C_{y\kappa}\, \arctan(B_{y\kappa}\, \kappa - E_{y\kappa}\, (B_{y\kappa}\, \kappa - \arctan(B_{y\kappa}\, \kappa)))) \tag{4.14}$$

The coefficients to the weighting function are computed from tire specific parameters and are dependent on vertical load.

$$\begin{aligned}
B_{y\kappa} &= r_{By1}\, \cos(\arctan(r_{By2}\, \alpha)) \\
C_{y\kappa} &= r_{Cy1} \\
E_{y\kappa} &= r_{Ey1} + r_{Ey2}\, df_z
\end{aligned}$$

Table 4.4 provides brief explanations to the lateral combined slip coefficients.

Coefficient	Description
r_{By1}	Slope factor for combined slip lateral force reduction
r_{By2}	Variation of slope lateral force reduction with α
r_{Cy1}	Shape factor for combined slip lateral force reduction
r_{Ey1}	Curvature factor of combined lateral force
r_{Ey2}	Curvature factor of combined lateral force with load

Table 4.4: Description of the lateral combined slip tire force coefficients.

The resultant lateral combined slip tire force F_y is given as the product of the pure slip tire force and weighting function.

$$F_y = F_{y0}\, G_{y\kappa}(\alpha,\, \kappa,\, F_z) \tag{4.15}$$

Figures 4.1 shows how the lateral and longitudinal forces vary with tire slip quantities α and κ for road friction $\mu = 1$, as modelled by the implemented modified PAC2002 model.

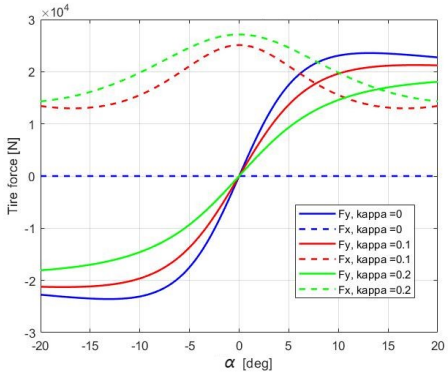

(a) Lateral tire force and lateral tire slip angle α for varying longitudinal slip ratio κ.

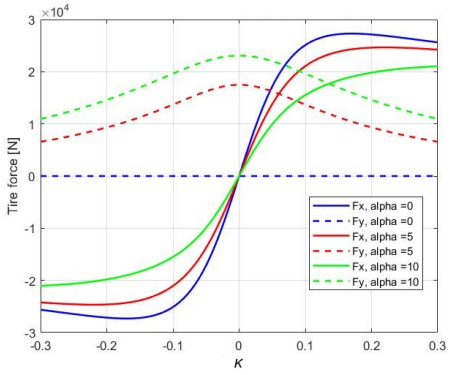

(b) Longitudinal tire force and longitudinal slip ratio κ for varying lateral tire slip angle α.

Figure 4.1: How lateral and longitudinal tire slip varies with tire slip quantities α and κ as modelled by the modified PAC2002 model.

The relationship between tire force and tire slip quantities is heavily dependent on the road friction coefficient, μ. There is also a dependence on the specific tire coefficients, which are found through testing. Figures 4.2 show plots of this relationship for varying road friction values, with specific tire coefficients from new tires and worn tires.

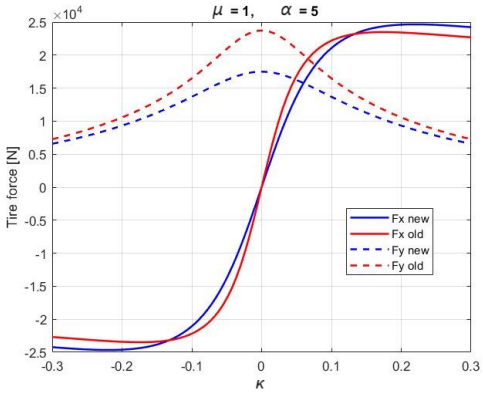

(a) Longitudinal tire force over κ, for road friction $\mu = 1$ and $\alpha = 5$ degrees.

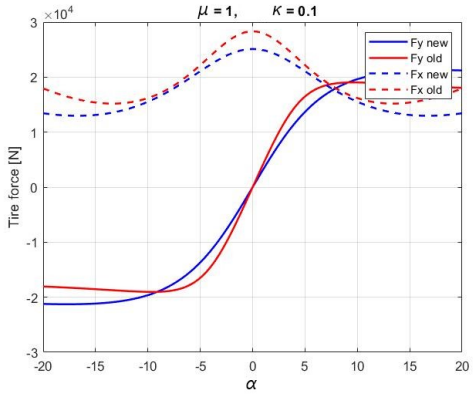

(b) Lateral tire force over α, for road friction $\mu = 1$ and $\kappa = 0.1$.

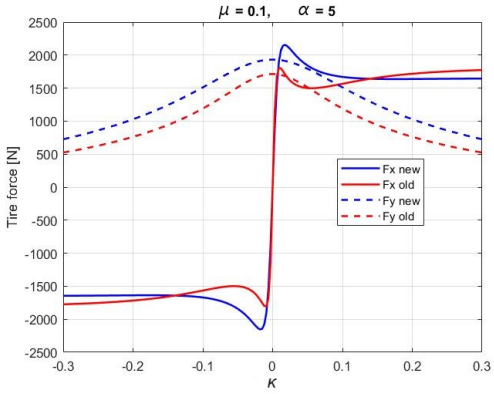

(c) Longitudinal tire force over κ, for road friction $\mu = 0.1$ and $\alpha = 5$ degrees.

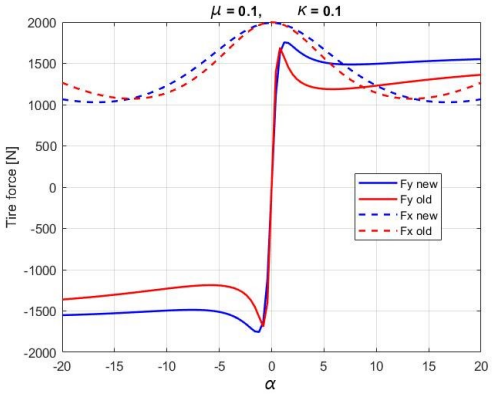

(d) Lateral tire force over α, for road friction $\mu = 0.1$ and $\kappa = 0.1$.

Figure 4.2: Relationship between tire force and tire slip quantities, for varying road friction levels and tire wear.

The weighting functions G_x and G_y as defined by the PAC2002 model are plotted in Figures 4.3, for varying vertical loads. While G_x is heavily dependent on normal load for larger values of α and κ, G_y remains almost independent of normal load. These were initially studied further with the motivation of deriving a simpler model for the tire forces, however it later became apparent that further simplification was not necessary for the sake of computation costs, and the weighting functions are defined, although slightly modified to neglect negligible aspects, from the PAC2002 model as presented in Equations 4.11 and 4.14.

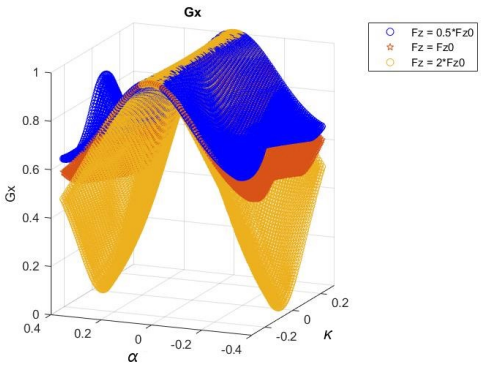

(a) Weighting function G_x for varying normal loads.

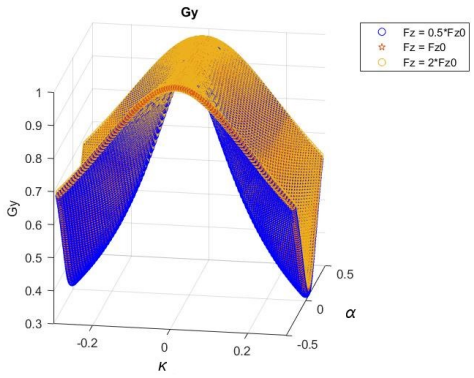

(b) Weighting function G_y for varying normal loads.

Figure 4.3: Weighting functions for varying normal loads.

5
Plant Modelling

The control system designed in this thesis has two main attributes. The first is a yaw controller which sends a request for difference in longitudinal slip ratios between the left and right side of the rear axle. The second and main part of the control system is a motion prediction which sends a request for negative longitudinal slip ratio to all four wheels of the vehicle to induce a breaking action. This section describes both the yaw controller and the motion prediction, as well as the chosen filter used mainly in the prediction for input signals from the driver interpreter.

Figure 5.1 shows an overview of the derived control system.

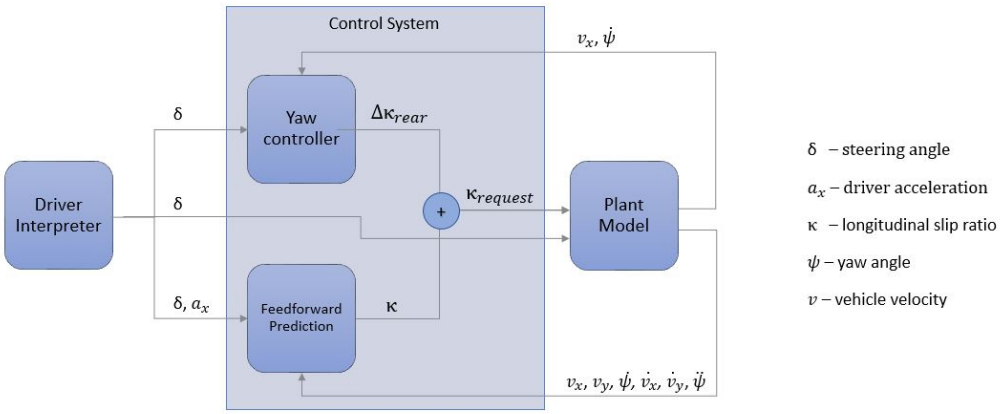

Figure 5.1: Motion prediction and yaw control system overview.

5.1 Yaw Control

One of the main objectives in this thesis is to avoid understeering. One way of dealing with this challenge is by introducing torque vectoring through a yaw controller [14]. Torque vectoring will allow for yaw control without noticeably affecting the velocity of the vehicle [12]. In many situations, however, additional breaking action may have to be applied to avoid understeering and provide additional yaw moment, which will be attended to by the motion prediction control described in Section 5.2 [4]. The yaw controller derived in this thesis is a Quantitative Feedback Design Theory (QFT) controller. The QFT controller follows a yaw reference generated by a linear tire model, derived from the PAC2002 model. The linear model is assumed to have unlimited tire forces available, thus making it idealistic, and has no longitudinal

dynamic.

5.1.1 Control allocation

A virtual torque was defined in Section 3.1.1, Equation 3.15. This is used to for longitudinal slip ratio allocation to each of the real tires, using a pseudo-inverse method [16].

$$\begin{aligned} T_v &= l_2\, K_{x2}(\kappa_{22}(t) - \kappa_{21}(t)) \\ &= \underbrace{\begin{bmatrix} -l_2\, K_{x2} & l_2\, K_{x2} \end{bmatrix}}_{\mathbf{B}} \begin{bmatrix} \kappa_{21} \\ \kappa_{22} \end{bmatrix} \end{aligned} \tag{5.1}$$

Pseudo inverse gives

$$\begin{bmatrix} \kappa_{21} \\ \kappa_{22} \end{bmatrix} = \mathbf{B}^*\, T_v \tag{5.2}$$

where

$$\mathbf{B}^* = (\mathbf{B}^T\, \mathbf{B}^{-1})\, \mathbf{B}^T \tag{5.3}$$

A limit to the longitudinal slip ratio of the rear tires is set as 80% of the peak value, as computed by a linear approximation of the Pac2002 pure slip tire model from the constant constraints D_{x2} and K_{x2} provided from tire testing.

$$\kappa_{2,lim} = 0.8\, \frac{D_{x2}}{K_{x2}} \tag{5.4}$$

The maximum limit to the virtual torque can then be defined.

$$\begin{aligned} T_{v,max} &= \begin{bmatrix} -l_2\, K_{x2} & l_2\, K_{x2} \end{bmatrix} \begin{bmatrix} -0.8\, \frac{D_{x2}}{K_{x2}} \\ 0.8\, \frac{D_{x2}}{K_{x2}} \end{bmatrix} \\ &= 1.6\, l_2\, D_{x2} \\ &\simeq 5000\text{Nm} \end{aligned} \tag{5.5}$$

5.1.2 QFT Controller Design

The QFT controller that was implemented in this thesis was primarily designed by a colleague at Volvo. A description of the controller design is given in this subsection, however credit for the design is to be given to Salmane Essayeh.

Quantitative Feedback Design Theory explicitly determines that desired loop properties are satisfied for a given model uncertainty. The QFT controller is generally less conservative than mother methods, such as the H_∞ method [7]. The synthesis of a controller using the QFT method is based on determining a value set of transfer functions in Nichols or Nyquist plots, for a set of frequencies. Specifications for the closed loop must then be satisfied for the value set at each frequency, which gives constraints to the controller frequency response. These constraints and specifications can be ensured through loop shaping analysis [11].

The QFT controller derived in this section is based on the transfer function between the yaw rate, $\dot{\psi}$, and the virtual torque, T_v, which is obtained by linearising the Simulink model. The linearised model is then used in the QFTC toolbox in Matlab to build a robust controller using a loop shaping method.

Figure 5.2 shows a block diagram of the controller design. $C(s)$ is the transfer function between the yaw rate, $\dot{\psi}$ and the virtual torque, T_v. The plant model $P(s)$ is the transfer function between the longitudinal slip ratio and the yaw rate. Y_{ref} is the reference yaw rate from the idealistic linear tire model. Y_{meas} is the measured sensor output. Y is the plant yaw rate output. The control effort U is the virtual torque. D_U is the control disturbance and D_Y is the output disturbance.

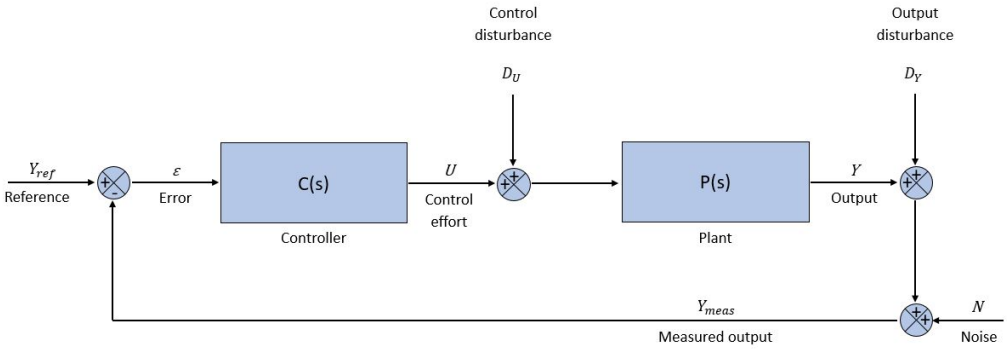

Figure 5.2: QFT controller design structure.

Firstly, the cross-over frequency needs to be determined, which fixes the controllers bandwidth. The cross-over frequency is determined based on the maximum control effort enforced by the noise.

$$\begin{aligned} \left|\frac{U}{N}\right| &= \left|\frac{C(s)}{1+P(s)C(s)}\right| \\ &\xrightarrow[s\to\infty]{} C(s) \\ &= C_0 < \left|\frac{u_{max}}{N_{max}}\right| \end{aligned} \tag{5.6}$$

The maximum control effort calculated in Equation 5.5 as $T_{v,max} \simeq 5000$ Nm. u_{max} is defined as the maximum control effort induced by noise, and is set as 10% of U_{max}. The maximum noise N_{max} is approximated as 10^{-4} rad/s. We can then determine C_0.

$$C_0 < 133\,\text{dB} \tag{5.7}$$

Figure 5.3 shows the Bode plot of the linearised model, and by choosing a value for C_0 which satisfies the constraint above, we can from the plot determine a cross-over frequency.

$$C_0 = 127\ \text{dB} \tag{5.8}$$

$$\omega_{cr} = 50\ \text{rad/s} \tag{5.9}$$

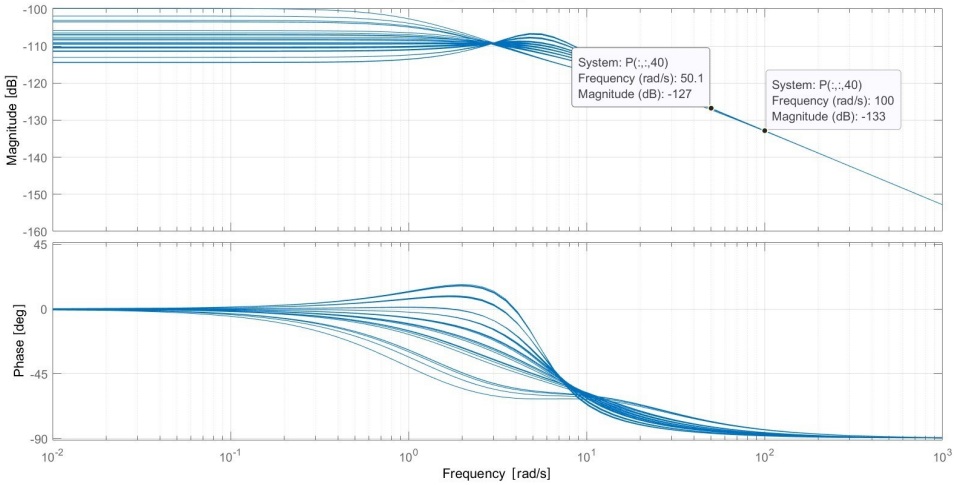

Figure 5.3: Bode plot with chosen cross over frequency.

Now we fix a set of frequencies around the cross-over frequency, for the loop shaping process of the QFT design, chosen as $\Omega = \{0.1, 0.51, 5, 10, 50, 80, 100, 200, 1000\}$. Figure 5.4 shows the plant templates plotted in Nichols chart. These templates represent the phase and gain uncertainties around the chosen set of frequencies Ω.

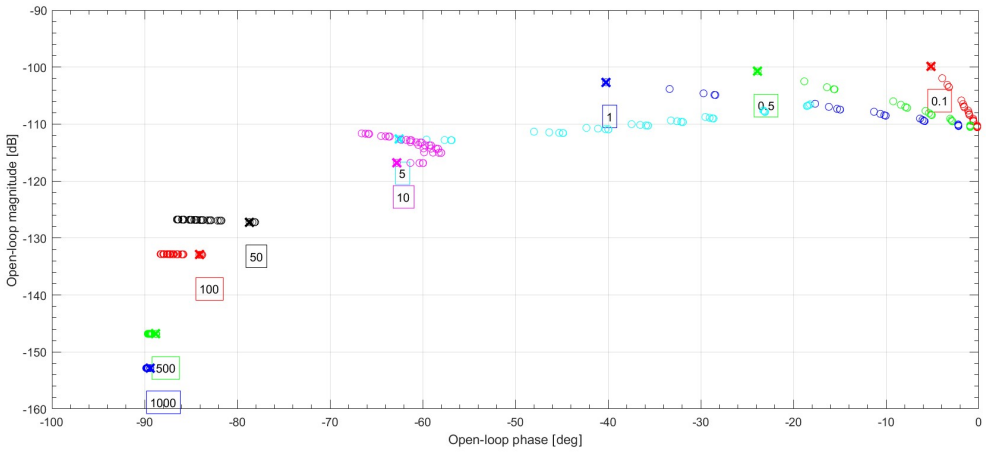

Figure 5.4: Plant templates in Nichols chart.

5.1.2.1 Loop Shaping and Frequency Domain Constraints

There are four frequency domain constraints to be satisfied in the design of the QFT controller [7]. These are the robust stability margin, the output disturbance rejection, the input disturbance rejection and the control effort limitation.

The robust stability margin is a constraint on the complementary sensitivity function and tracking performance.

$$\left|\frac{C(s)P(s)}{1+C(s)P(s)}\right| \leq W_1 \tag{5.10}$$

This constraint is fixed in the time domain as limiting the overshoot below 20%, which enables a resonance faction of the T function Q_T below 3dB = W_1. Figure 5.5a shows this constraint as satisfied.

The output disturbance attenuation is a constraint on sensitivity function.

$$|\frac{1}{1+C(s)P(s)}| \leq W_2 \tag{5.11}$$

This constraint ensures a response time as small as possible and a relative error of less than 1% for steady state accuracy. There are two conditions that must be satisfied to ensure this constraints. The first is to affirm a low gain in low frequencies to secure the rejection of the output disturbance. We can show that this is satisfied since the sensitivity function goes to zero through the final value theorem.

$$\begin{aligned} \lim_{t\to\infty}\left|\frac{Y}{D_U}\right| &= \lim_{s\to 0} sS(s) \\ &\leq sW_2(s) \\ &= 0 \end{aligned} \tag{5.12}$$

The second condition to be satisfied is the resonance factor of the sensitivity function $S(s)$. We want to ensure a modulus margin of at least 0.5, $M_M > 0.5$, which is secured by a 6 dB high frequency gain.

$$|S(s) = \left|\frac{1}{1+P(s)C(s)}\right| \tag{5.13}$$

$$\max|S(s)| = \frac{1}{\min|1+P(s)C(s)|} \tag{5.14}$$

$$\min|1+P(s)C(s)| = \frac{1}{\max|S(s)|} \tag{5.15}$$

Since the limit is set such that $\max|S(s)| < W_2 = 6$ dB $\simeq 2$, we ensure a modulus margin of at least 0.5.

$$M_M = \min|1+P(s)C(s)| > \frac{1}{2} \tag{5.16}$$

Figure 5.5b shows this constraint as satisfied.

The third constraint is the input disturbance rejection. This constraint is handled directly by the QFT Toolbox by adding an integral action in the loop shaping process, as presented in [6]. Figure 5.5c shows that this constraint is satisfied.

$$|\frac{G(s)}{1+C(s)P(s)}| \leq W_3 \tag{5.17}$$

The fourth and final constraint is the control effort limitation, which ensures that the limit of the control effort, $T_{v,max}$, is fixed at 5000 Nm, and that the sensitivity of the control to measurement noise does not exceed 10% of the control effort.

$$|\frac{C(s)}{1+C(s)P(s)}| \leq W_4 \tag{5.18}$$

This constraint has been set as $W_4 = 127$ dB from the determination of the crossover frequency in Equation 5.8. Figure 5.5d shows this constraint as satisfied.

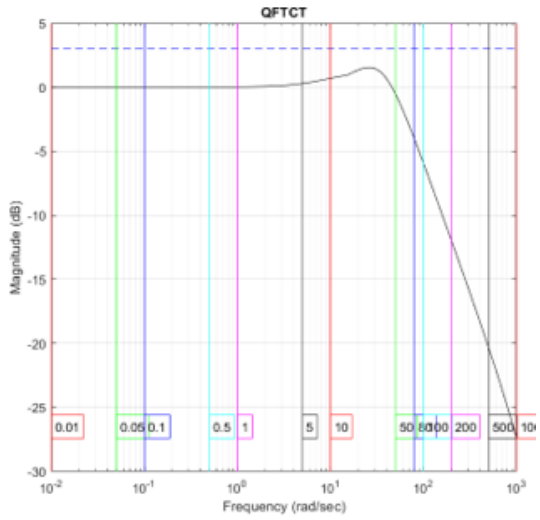

(a) Robust stability margin (solid) and its constraint W_1 (dashed line).

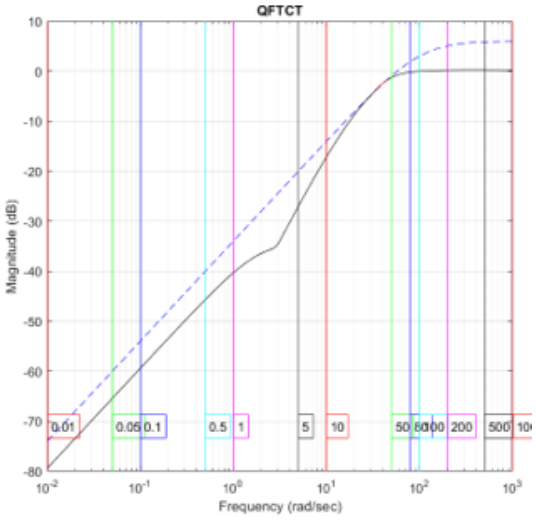

(b) Output disturbance rejection (solid line) and its constraint W_2 (dashed line).

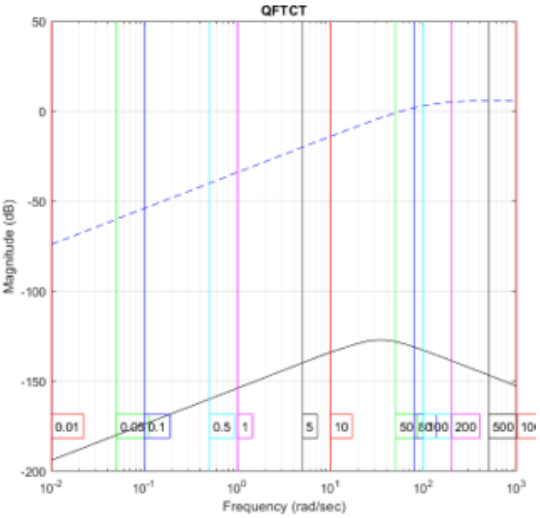

(c) Input disturbance rejection (solid line) and its constraint W_3 (dashed line).

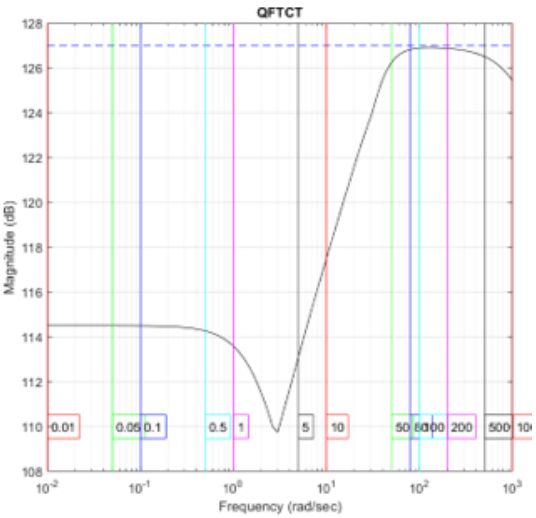

(d) Control effort limitation (solid line) and its constraint W_4 (dashed line).

Figure 5.5: Frequency domain constraints analysis.

With the plant templates and the frequency domain constraints established, the next step is to perform a loop shaping in the QFTC toolbox in Matlab. The QFTC toolbox plots an intersection of the boundaries of each of the frequencies in the chosen set Ω around our cross over frequency. This provides upper and lower boundaries for each frequency, and the loop shaping process ensures these are satisfied. Figure 5.6a shows the boundaries prior to the loop shaping process. The solid lines are boundaries for which the frequency points need to be above, and the dashed lines are boundaries for which the frequency points need to be below, for a robust con-

troller. Figure 5.6b shows these boundaries and frequency points after completing the loop shaping.

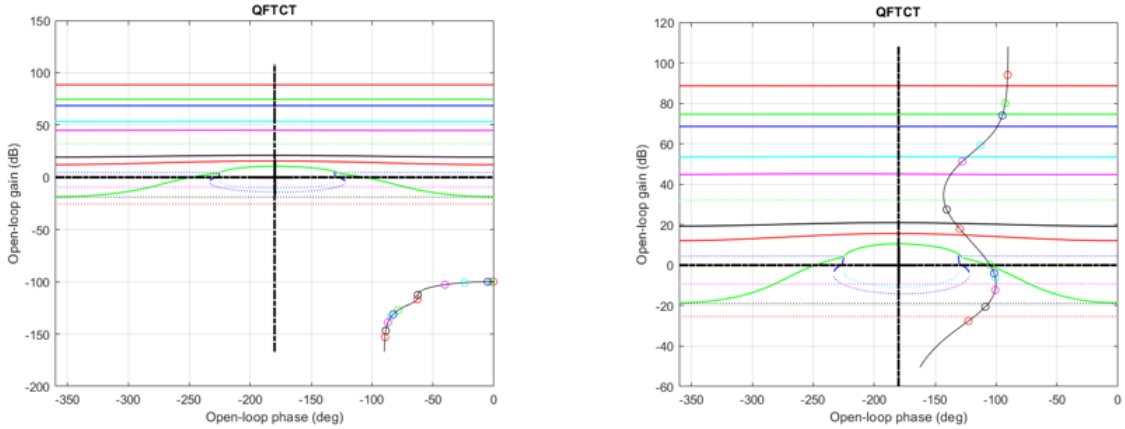

(a) Open loop.

(b) Loop shaping completed.

Figure 5.6: QFT controller loop shaping.

An integrator is added in the loop shaping, to handle the third constraint on input disturbance rejection, D_U, and the gain is adjusted to fit the boundaries of the loop shaping. A phase shift is then added by adding a zero at the frequency 28.26 rad/s, which then satisfies all boundaries. The resultant transfer function is now given as

$$C(s) = C_0 \frac{1}{s}\left(1 + \frac{s}{\omega_{zero}}\right) \tag{5.19}$$

In order to make the controller more robust, we also introduce a pole in high frequencies $\omega = 1000$ rad/s, which will allow for filtering at high frequencies. This will make our transfer function into a strictly proper transfer function, given as

$$C(s) = \frac{2.154 \cdot 10^6\, s + 4.955 \cdot 10^7}{0.0004\, s^2 + s} \tag{5.20}$$

The final step is to split the controller into proportional and integral parts, thus allowing the integrator part to be used in anti-windup.

$$C(s) = \frac{5.3358 \cdot 10^9}{s + 2500} + \frac{4.955 \cdot 10^7}{s} \tag{5.21}$$

Figure 5.7 shows the step response of the final QFT controller. The step response does not exceed 20% as ensured by the robust stability margin.

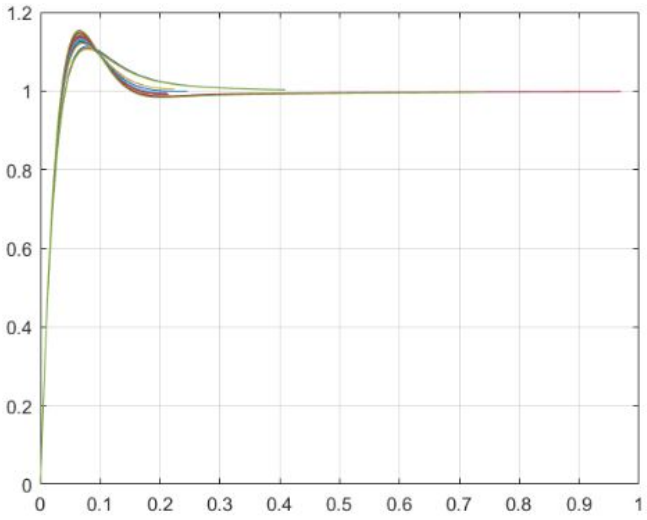

Figure 5.7: Step response for the QFT controller.

5.2 Motion Prediction and Velocity Control

The prediction model uses the vehicle and tire models presented in Chapters 3.1.1 and 4.1. The prediction horizon is $T = 2$ seconds ahead. A longer prediction horizon will get a better result, however the extrapolation of the inputs may vary significantly from the actual inputs for a longer horizon. Additionally, a longer horizon either provides a heavier computation cost, or if the sampling time is increased, may reduce the accuracy. The sampling time in the prediction is set to $dt = 0.01$.

Three critical limits are defined for the prediction model. The first is a limit to the longitudinal tire slip, κ_{lim}. The second is a limit to the maximum lateral tire forces physically available for the vehicle, $\sum F_{y,max}$. The third is a limit to the lateral force of the vehicle, $\Gamma_{y,lim}$. The prediction plant uses these as critical limits for when deceleration of the vehicle is necessary to stay within safe driving conditions. If the plant predicts that these limits may be exceeded, a negative longitudinal slip request $\kappa_{request}$ is sent, and the velocity of the vehicle is reduced according to equations presented in the respective sections below. If several limits are reached within the prediction, then the most conservative calculated action is implemented to the vehicle.

5.2.1 Longitudinal Tire Slip Limit

The longitudinal tire slip limit, κ_{lim}, is set as 80% of the Pacejka peak factor divided by the slip stiffness. This limit is set to keep the vehicle within the linear part of the tire force plot, which maintains normal tire force conditions. The safety scale factor of 80% is to avoid overshooting the limit in case of uncertainties or rapid changes in road conditions.

$$\kappa_{lim} = 0.8 \frac{D_x}{K_x} \tag{5.22}$$

If this limit is reached during a prediction, a calculation of the required vehicle velocity and subsequent deceleration is then done, based on the current vehicle states and road friction level and how far ahead within the prediction horizon the limit is reached, according to Algorithm 1.

Algorithm 1 Longitudinal slip limit

for t within prediction horizon **do**
  $\kappa \leftarrow \{v_x, v_y, \dot{\psi}, \dot{v}_x, \dot{v}_y, \ddot{\psi}, \delta, a_{x,driver}\}_t$ ▷ Update κ from states
  if $\kappa \geq \kappa_{lim}$ **then**
    $R = \sqrt{(\frac{L}{\tan\delta})^2}$
    $v_{x,req} = \sqrt{\mu\, g\, R}$
    $t_{crit} = t$
    $a_{x,req} = \frac{v_{x,req} - v_x}{t_{crit}}$
  end if
  $\{v_x, v_y, \dot{\psi}, \dot{v}_x, \dot{v}_y, \ddot{\psi}, \delta, a_{x,driver}\}_t \leftarrow \{v_x, v_y, \dot{\psi}, \dot{v}_x, \dot{v}_y, \ddot{\psi}, \delta, a_{x,driver}\}_{t+dt}$ ▷ Update states
end for

R is the radius to centre of turning circle imposed by steering angle δ. L is the length between the front and rear axles. t is the time within the prediction iteration.

5.2.2 Maximum Lateral Tire Force Limit

The maximum tire force of the vehicle is the theoretical maximum lateral force available, according to the implemented tire model, and is defined as the sum of the lateral tire peak factors, D_y. A vehicle which has reached this limit will have saturated the available lateral tire force and is at critical risk of understeering.

$$\sum F_{y,max} = \sum_{j,n} D_{y,jn} \tag{5.23}$$

$j = 1, 2$ is the axle and $n = R, L$ is the right or left side tire. If this limit is reached during a prediction then a calculation of the required vehicle velocity and subsequent deceleration is done, according to Algorithm 2.

Algorithm 2 Lateral force limit

for t within prediction horizon **do**
  $\Gamma_y \leftarrow \{v_x, \dot{\psi}, \dot{v}_y\}_t$ ▷ Update Γ_y from states
  if $\Gamma_y \geq \sum F_{y,max}$ **then**
    $v_{x,req} = 0.5\, \frac{\sum F_{y,max} - \dot{v}_y}{\dot{\psi}}$ ▷ Scale security factor 0.5
    $t_{crit} = t$
    $a_{x,req} = \frac{v_{x,req} - v_x}{t_{crit}}$
  end if
  $\{v_x, \dot{\psi}, \dot{v}_y\}_t \leftarrow \{v_x, \dot{\psi}, \dot{v}_y\}_{t+dt}$ ▷ Update states
end for

5.2.3 Lateral Force Limit

The lateral force limit, $\Gamma_{y,lim} = 0.35\,g$ is a limit at which the vehicle is in critical risk of rollover. If this limit is reached during a prediction then a calculation of the required vehicle velocity and subsequent deceleration is done, according to Algorithm 3.

Algorithm 3 Lateral force limit

for t within prediction horizon **do**
  $\Gamma_y \leftarrow \{v_x, \dot{\psi}, \dot{v}_y\}_t$ ▷ Update Γ_y from states
  if $\Gamma_y \geq \Gamma_{y,lim}$ **then**
    $v_{x,req} = 0.5\,\frac{\Gamma_{y,lim} - \dot{v}_y}{\dot{\psi}}$ ▷ Scale security factor 0.5
    $t_{crit} = t$
    $a_{x,req} = \frac{v_{x,req} - v_x}{t_{crit}}$
  end if
  $\{v_x, \dot{\psi}, \dot{v}_y\}_t \leftarrow \{v_x, \dot{\psi}, \dot{v}_y\}_{t+dt}$ ▷ Update states
end for

5.2.4 Savitzky–Golay Filtering and Smoothing

Some filtering is included in the prediction model to account for noise and to provide a reliable extrapolation of the driver interpreter inputs for the motion prediction. In this thesis the Savitzky-Golay filter has been investigated and implemented for this application, and was suggested by supervisors at Volvo Group Truck Technology since this type of filter is used in other applications of the vehicle.

The Savitzky-Golay filter is a moving average type filter which also provides a derivative for every filtered output, and is therefore useful for extrapolating states when running a prediction algorithm [10][23]. The filter computes two sets of constant filter coefficients based on chosen parameters, and is therefore a good fit for real-time implementation since no further computation needs to be conducted during implementation.

5.2.4.1 Smoother

The Savitzky-Golay smoother is a moving average type filter which fits a polynomial to an odd set of m data points, separated by an interval h, by the linear least squares method. The filter defines a new variable z from the central point $\bar{x}$, according to 5.24.

$$z = \frac{x - \bar{x}}{h} \tag{5.24}$$

The new variable takes on the values $z = \{\frac{1-m}{2}, \ldots, 0, \ldots, \frac{m-1}{2}\}$, such as for $m = 5$, this vector would become $z = \{-2, -1, 0, 1, 2\}$.

A polynomial of degree p and its derivative is defined, with coefficients a_j, according to 5.25 and 5.26. Further derivatives of order up to p may be obtained accordingly.

$$\begin{aligned} Y &= a_0 + a_1 z + a_2 z^2 + \cdots + a_p z^p \\ \frac{dY}{dx} &= \frac{1}{h}(a_1 + 2a_2 z + 3a_3 z^2 + \cdots + p a_p z^{p-1}) \end{aligned} \tag{5.25}$$

$$\boldsymbol{a} = (\boldsymbol{J}^T \boldsymbol{J})^{-1} \boldsymbol{J}^T \boldsymbol{y} \tag{5.26}$$

$\boldsymbol{J}$ is the Vandermonde matrix. The m:th row of the Vandermonde matrix takes values $1, z_m, z_m^2, \ldots$, such that for $m = 5$ this matrix becomes

$$\boldsymbol{J} = \begin{bmatrix} 1 & z_1 & z_1^2 & \ldots & z_1^{p-1} \\ 1 & z_2 & z_2^2 & \ldots & z_2^{p-1} \\ 1 & z_3 & z_3^2 & \ldots & z_3^{p-1} \\ \vdots & \vdots & \vdots & \ddots & \vdots \\ 1 & z_m & z_m^2 & \ldots & z_m^{p-1} \end{bmatrix} \tag{5.27}$$

$$\boldsymbol{J} = \begin{bmatrix} 1 & -2 & 4 & 8 \\ 1 & -1 & 1 & -1 \\ 1 & 0 & 0 & 0 \\ 1 & 1 & 1 & 1 \\ 1 & 2 & 4 & 8 \end{bmatrix} \tag{5.28}$$

We then get the coefficients a_j, for $m = 5$.

$$a_{0,j} = \frac{1}{35}(-3y_{j-2} + 12y_{j-1} + 17y_j + 12y_{j+1} - 3y_{j+2}) \tag{5.29}$$

$$a_{1,j} = \frac{1}{12}(y_{j-2} - 8y_{j-1} + 8y_j - y_{j+2}) \tag{5.30}$$

$$a_{2,j} = \frac{1}{14}(2y_{j-2} - y_{j-1} - 2y_j - y_{j+1} + 2y_{j+2}) \tag{5.31}$$

$$a_{3,j} = \frac{1}{12}(-y_{j-2} + 2y_{j-1} - 2y_{j+1} + y_{j+2}) \tag{5.32}$$

The coefficients of y in the expressions for the coefficients a_j are named the convolution coefficients, and can be found as the elements in the convolution matrix.

$$\boldsymbol{C} = (\boldsymbol{J}^T \boldsymbol{J})^{-1} \boldsymbol{J}^T \tag{5.33}$$

This matrix gives an expression for the polynomial Y

$$(C \times y)_j = Y_j = \sum_{i=\frac{1-m}{2}}^{\frac{m-1}{2}} C_i y_{j+2} \tag{5.34}$$

where $\frac{m+1}{2} \leq j \leq n - \frac{m-1}{2}$, $j = 1, ..., n$.

The filtered value of the central point is found at $z = 0$ and $\bar{x} = x$. From 5.25 we then get that the smoothed data point is obtained from the coefficient a_0, and the first derivative is obtained from the the coefficient a_1.

$$Y = a_0 \tag{5.35}$$

$$\frac{dY}{dx} = \frac{1}{h} a_1 \tag{5.36}$$

5.2.4.2 Filter

The Savitzky-Golay filter is used similarly to the smoother as a filter in real time when only previous values are known. The data vector z now takes on only previous values, such that for $m = 5$ this vector becomes $z = \{-4, -3, -2, -1, 0\}$. By defining the order of the polynomial Y as at least one we get the derivative of the filtered output, which can then be used for extrapolation in the motion prediction.

Figure 5.8 shows Savitzky-Golay filtered signals from the driver interpreter sensors.

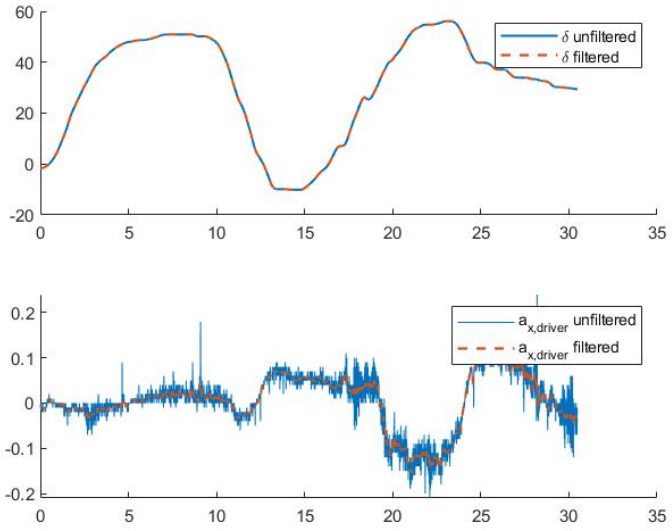

Figure 5.8: Unfiltered and Savitzky-Golay filtered signals δ and a_x from driver interpreter.

The steering angle δ sensor signals from the driver interpreter has very low noise levels. Thus, the amount of filtering needed is not very significant, however filtering is especially valuable in order to procure a reliable extrapolation of the input signals. The pedal action a_x sensor signal has significant noise, and filtering is necessary. From simulation and testing it was found that a Savitzky-Golay filter of low order, although of at least 1 to provide a filter derivative, gave the best filter and extrapolation results. A large window is evidently preferred for extrapolation, however this has a trade-off with increased computation time. Testing and simulation found that, since the filter coefficients are computed offline, the computation time is generally low for a window of approximately 10, and generates accurate results.

The chosen filter used in this thesis is of window 10 and order 1. This is chosen by running simulation with various setups to find the best filter in terms of computation

time and accuracy. With order 1 and window 10 we get the coefficients a_j.

$$a_0 = [-0.1455, -0.0909, -0.0364, 0.0182, 0.0727, 0.1273, 0.1818, 0.2364, 0.2909, 0.3455]\mathbf{y} \tag{5.37}$$

$$a_1 = [-0.0545, -0.0424, -0.0303, -0.0182, -0.0061, 0.0061, 0.0182, 0.0303, 0.0424, 0.0545]\mathbf{y} \tag{5.38}$$

We then get the filtered signal Y from a set of previous signal input values $\mathbf{y}$, as well as the filtered derivative used for extrapolation in the motion prediction.

$$Y = a_0 \tag{5.39}$$

$$\frac{dY}{dx} = \frac{1}{h}a_1 \tag{5.40}$$

6
Simulation

Simulations of the derived model are run in C++. The simulations have been compared to established vehicle models VTM and VCPP derived by Volvo Group Truck Technology to ensure the modelling of the vehicle is coherent.

The test case presented in this thesis is a turn with radius 90 m, run for varying initial velocities and road frictions. The turning scenario tests the models ability to prevent rollover and understeer, with results tables presented in this section. Some criteria have been established to give a pass or fail grade for each simulation, for the cases of understeer and rollover. Rollover criteria fails when the vehicle reaches lateral force over the critical limit 0.35 g. Understeer fails when the vehicle has reared off the lane, which is at path deviation larger than 1.25 m, using the minimum lane width in Europe at 2.5 meters [9].

Figures 6.1-6.4 show simulation results for a turning scenario with an initial velocity of 70 km/h on wet asphalt, $\mu = 0.7$. The initial steering is zero, a ramp increase starts at 3 seconds and the maximum and constant steering is reached at 6 seconds and is kept until the simulation is ended at 20 seconds. The vehicle is simulated as free rolling, i.e. no velocity control and no driver acceleration input is implemented. Figures 6.1-6.4 show simulation results for various states with simulations run with the yaw controller enabled and disabled and the motion prediction enabled and disabled. The open loop simulation, where motion prediction and yaw control are disabled, does not complete the simulation. This scenario reaches the rollover limit at approximately 6 seconds, and also severely drifts. Simulation with the yaw controller enabled does maintain stable yaw control, however this scenario as well reaches rollover limit, although this is realistically inevitable at this velocity. Simulation with motion prediction control enabled avoids both understeer and rollover. Simulation with both motion prediction control and yaw controller enabled achieves the best results.

Figure 6.1 shows the longitudinal slip ratios κ during the turning scenario simulation. The open loop simulation does not implement any control to κ, and is not able to finish the simulation which is stopped at around 10 seconds, due to rollover and severe drifting. The yaw controller enables a virtual torque to the rear wheels, to maintain yaw control. Simulation with prediction enabled implements a breaking action at 3 seconds, as soon as the steering is activated, and reaches maximum breaking action around 6 seconds, when maximum steering is reached. As the vehicle slows and the steering reaches a constant input, the breaking action diminishes until

at around 14 seconds, when a stable velocity is reached for the prediction. Simulation with both prediction and yaw control implemented shows a combined result of the two controllers. This simulation has a slightly lower maximum breaking action than the prediction used independently, and the vehicle reaches a stable velocity where no further breaking action is implemented slightly sooner, at around 13 seconds.

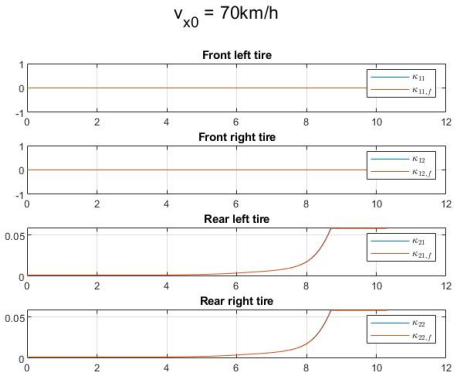

(a) Prediction and yaw control disabled.

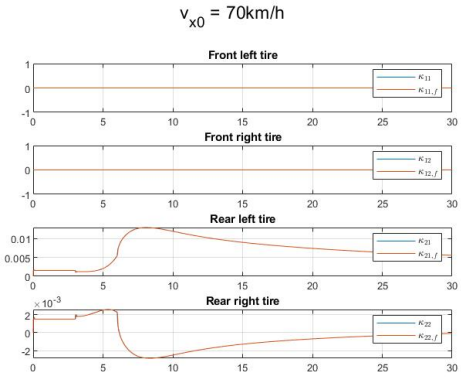

(b) Yaw controller enabled.

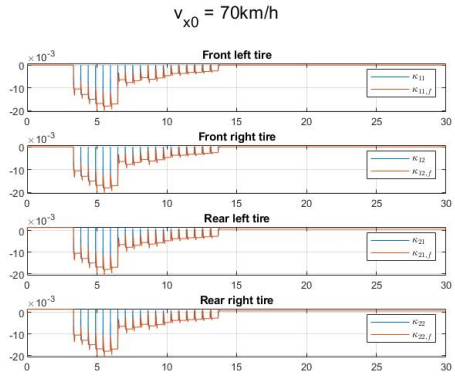

(c) Prediction control enabled.

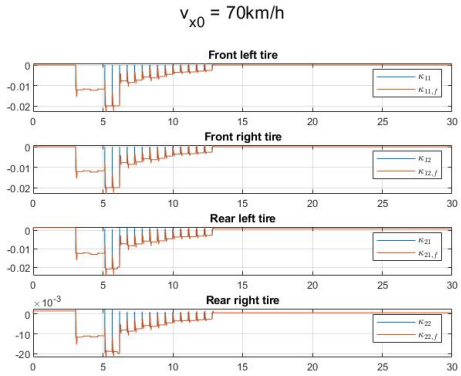

(d) Prediction and yaw control enabled.

Figure 6.1: Longitudinal slip ratio, κ, during turning scenario simulation.

Figure 6.2 shows the yaw rate $\dot{\psi}$ during the turning scenario simulation. The open loop simulation is not able to follow the yaw reference and a rapid increase in yaw rate suggests this vehicle has started spinning. Simulation with the yaw controller enabled follows the yaw reference completely. The simulation with the prediction control enabled is also able to follow the yaw reference very well by managing velocity to maintain sufficient available tire forces, although not precisely. With both prediction and yaw control enabled, the yaw reference is again followed completely, and this simulation results in a slightly lower maximum yaw rate.

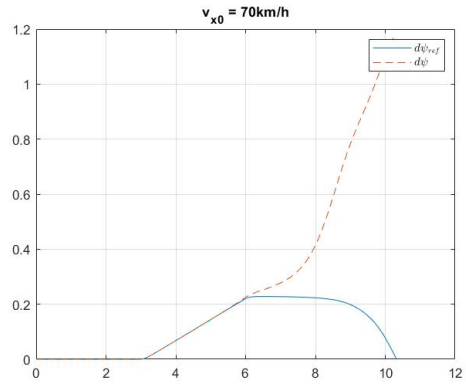

(a) Prediction and yaw control disabled.

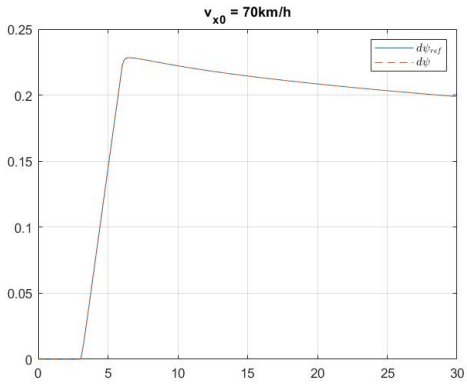

(b) Yaw controller enabled.

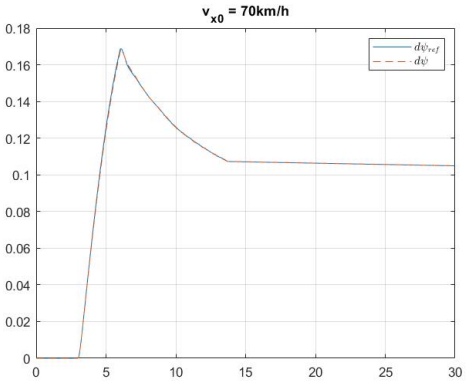

(c) Prediction control enabled.

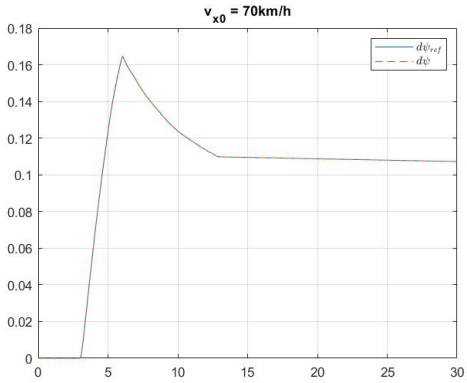

(d) Prediction and yaw control enabled.

Figure 6.2: Yaw rate, $\dot{\psi}$, during turning scenario simulation.

Figure 6.3 shows the longitudinal and lateral velocities v_x and v_y during the turning scenario simulation. Simulations are programmed to stop if longitudinal velocity hits zero, which occurs at around 10 seconds during the open loop simulation. In this case, the lateral velocity is very large when simulation is stopped, suggesting once more that this vehicle has started spinning. The rapid changes in longitudinal and lateral velocities occur very shortly after the steering is initiated, thus the vehicle loses grip only seconds after steering is introduced. The simulation with yaw control enabled shows that the longitudinal velocity drops somewhat to ca 61 km/h. There is some lateral velocity induced, however the lateral velocity decreases after an initial peak as the maximum steering is reached. The two final simulations with prediction enabled and with prediction and yaw control in combination give similar results. The longitudinal velocity is quickly decreased to around 35 km/h, after which the vehicle is free rolling. There is a slight decrease in the deceleration after maximum steering is reached at 6 seconds. The final velocity is quite low. By tuning some scaling factors the deceleration action can be made less strict. Evaluation of how conservative the prediction control should be will have to be done as a future work, since simulation results suggest that this model may be too restrictive. There is also a change in direction of lateral acceleration, induced by centripetal forces. The prediction and yaw control combination results in slightly higher final longitudinal

velocity and slightly lower overall lateral velocity than the prediction control run independently.

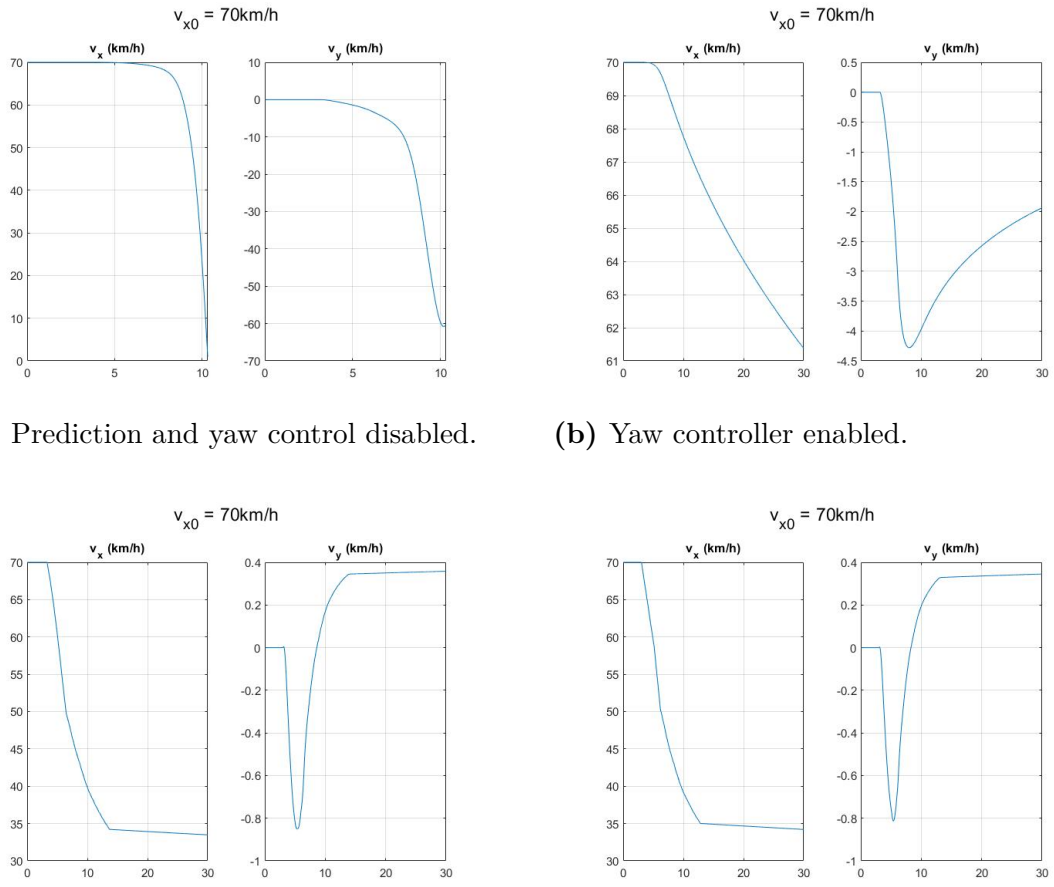

(a) Prediction and yaw control disabled.

(b) Yaw controller enabled.

(c) Prediction control enabled.

(d) Prediction and yaw control enabled.

Figure 6.3: Velocities during turning scenario simulation.

Figure 6.4 shows the lateral force Γ_y during the turning scenario simulation. The simulations are not stopped once the critical rollover limit is reached. The open loop simulation significantly exceeds the lateral force limit, and it can be concluded that this simulation ends in a rollover situation. Although the simulation with yaw control enabled does not reach as high lateral force as the open loop, it is still far past the limit. This limit is is some cases quite conservative depending on how the vehicle is loaded, which is not yet taken into account in model, however in this thesis this is considered as a failed simulation. The simulations with prediction enabled and with prediction and yaw control in combination do not get near the limit. This suggests that the prediction control may be unnecessarily conservative and some tuning of the prediction is necessary.

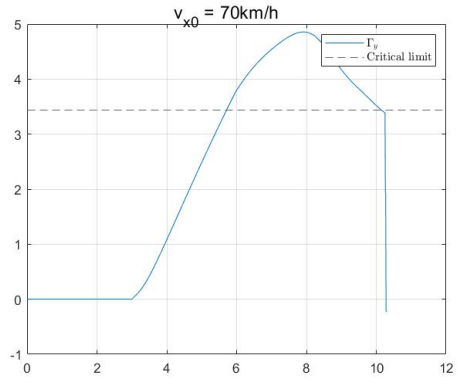

(a) Prediction and yaw control disabled.

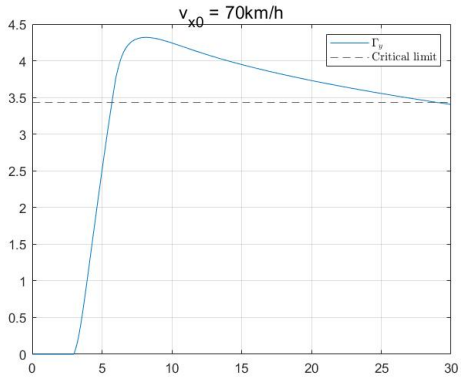

(b) Yaw controller enabled.

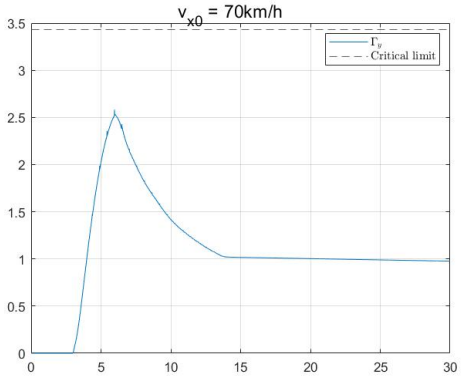

(c) Prediction control enabled.

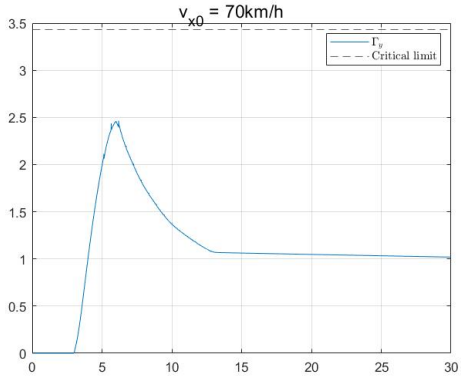

(d) Prediction and yaw control enabled.

Figure 6.4: Lateral force, Γ_y, during turning scenario simulation.

Figure 6.5 shows the vehicles path during the turning scenario simulation, alongside an idealistic path from a linear model with unlimited tire forces available. Simulation of the open loop system shows only a small path deviation, however we know from other states that this vehicle has lost traction and has overturned. The simulation with yaw control enabled follows the path quite well, however it does deviate more than half a lane width (1.25m), which is the maximum allowed deviation in this thesis, thus the understeering is deemed too high. Both simulations with prediction control individually and prediction in combination with yaw control enabled follow the path without deviating too far. However, the simulation with only prediction control enabled does deviate almost twice as much as the simulation with additional yaw control enabled.

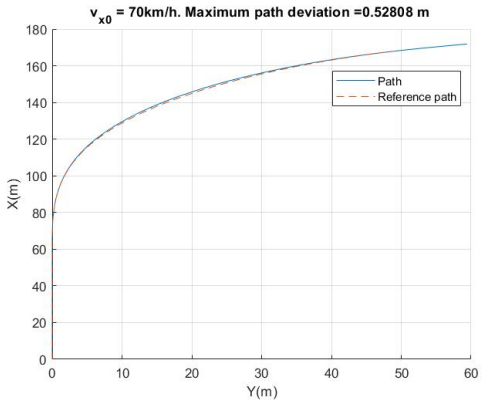

(a) Prediction and yaw control disabled.

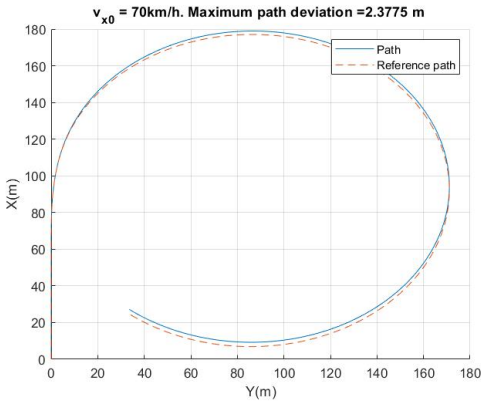

(b) Yaw controller enabled.

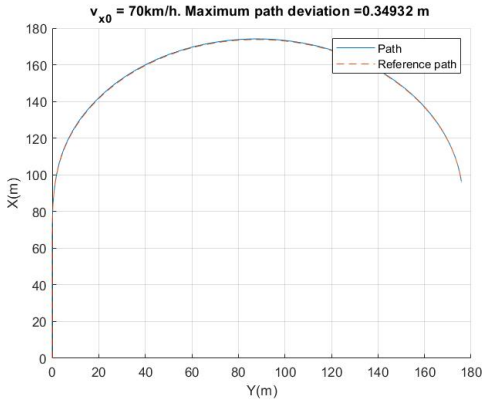

(c) Prediction control enabled.

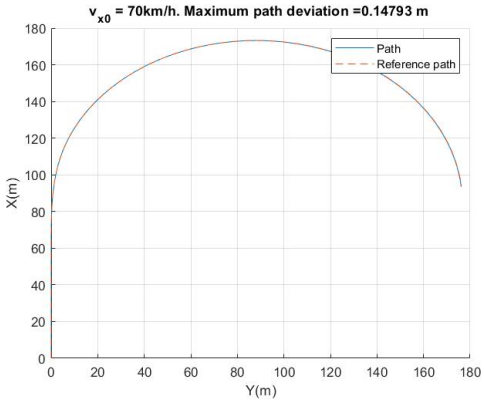

(d) Prediction and yaw control enabled.

Figure 6.5: Vehicle path during turning scenario simulation.

6.1 Performance Tables

This section presents performance tables for simulations run at four variations of road friction μ, with varying initial velocities. The same turning scenario as presented previously is applied, a circular path with a 90 m radius. Criteria have been set for either a pass or a fail for understeer and rollover. A simulation has failed to avoid understeer if the path deviation exceeds half a lane with, >1.25 m, or if the vehicle has started to turn around due to loss of tire traction. A simulation has failed to avoid rollover if the lateral force critical limit of 0.35 g has been exceeded. A simulation which has not been given a value for final velocity in the performance tables has stopped due to loss of traction.

Table 6.1: Performance table for simulation on ice, μ=0.1

v_{x0}	**Criteria**	**Open loop**	**Feedback**	**Feedforward**	**FB & FF**
20	$\dot{\psi}_{max}$	0.0621	0.0621	0.0621	0.0597
25		0.0786	0.0773	0.0742	0.0670
30		0.3820	0.0931	0.0797	0.0733
35		0.4403	0.4375	0.0892	0.0837
40		0.4907	0.5141	0.3714	0.0978
45		0.5304	0.5669	0.4463	0.1133
20	$a_{y,max}$	0.3746	0.3763	0.3746	0.3504
25		0.5532	0.5515	0.5173	0.4311
30		0.6948	0.6974	0.5836	0.5072
35		0.4802	0.5358	0.6675	0.6326
40		0.4656	0.4748	0.6919	0.7006
45		0.4499	0.4529	0.4922	0.7031
20	*Path offset*	0.0322	0.0226	0.0322	0.0261
25		1.5458	0.1467	0.4977	0.0495
30		13.2087	24.7716	0.4869	0.0600
35		17.2973	13.0978	1.0819	0.0650
40		13.9089	16.3710	11.9052	0.1678
45		11.3397	17.7797	21.9936	18.0282
20	$v_{x,final}$	19.6105	19.6074	19.6105	18.8668
25		24.3861	24.2268	21.3399	20.9893
30		-	21.1513	21.3288	21.2033
35		-	-	21.5969	21.8157
40		-	-	-	21.7362
45		-	-	-	17.4853
20	*Fail*	0	0	0	0
25		US	0	0	0
30		US	US	0	0
35		US	US	0	0
40		US	US	US	0
45		US	US	US	US

Table 6.2: Performance table for simulation on snow, μ=0.3

v_{x0}	**Criteria**	**Open loop**	**Feedback**	**Feedforward**	**FB & FF**
30	$\dot{\psi}_{max}$	0.0937	0.0936	0.0937	0.0899
40		0.1277	0.1257	0.1277	0.1153
50		0.7118	0.1587	0.1378	0.1229
60		0.8246	0.1925	0.1555	0.1401
70		0.9166	0.2267	0.6906	0.1568
80		0.9888	0.8544	0.8334	0.1851
30	$a_{y,max}$	0.8028	0.8054	0.8028	0.7493
40		1.4131	1.3900	1.7429	1.1749
50		2.0803	2.0907	1.6444	1.3521
60		1.5206	2.1031	1.9241	1.7249
70		1.4220	2.1075	2.0742	2.0291
80		1.3221	2.0434	1.6089	2.0998
30	*Path offset*	0.1710	0.0375	0.1552	0.0620
40		2.4198	0.2471	0.5297	0.1380
50		12.7961	3.5213	0.6014	0.1414
60		16.0084	62.9403	2.4585	0.2759
70		15.4058	124.4745	11.8778	0.7531
80		14.6957	15.9266	19.6389	13.2555
30	$v_{x,final}$	29.1476	29.1349	29.1476	28.0592
40		38.4019	38.3764	34.6500	35.4647
50		-	45.7618	29.8788	29.4348
60		-	29.4814	30.1774	29.7279
70		-	26.3038	-	30.2314
80		-	-	-	29.9867
30	*Fail*	0	0	0	0
40		US	0	0	0
50		US	US	0	0
60		US	US	US	0
70		US	US	US	0
80		US	US	US	US

Table 6.3: Performance table for simulation on wet asphalt, μ=0.7

v_{x0}	**Criteria**	**Open loop**	**Feedback**	**Feedforward**	**FB & FF**
40	$\dot{\psi}_{max}$	0.1259	0.1257	0.1259	0.1206
50		0.1600	0.1588	0.1486	0.1185
60		0.2000	0.1929	0.1594	0.1360
70		1.1722	0.2283	0.1679	0.1513
80		1.3832	0.2647	0.1876	0.1705
90		1.5369	0.3018	0.1877	0.1707
100		1.6537	1.1369	0.2108	0.1780
110		1.7500	1.3574	1.3131	0.1937
40	$a_{y,max}$	1.3947	1.3929	1.3947	1.2891
50		2.2108	2.1939	1.9560	1.2741
60		3.3037	3.1855	2.2700	1.6567
70		4.8572	4.3166	2.5828	2.0508
80		3.8999	4.8412	3.4253	2.6514
90		3.4890	4.8473	3.7106	2.8357
100		3.1135	4.8818	4.2450	3.4209
110		2.7166	3.8423	4.8657	3.9001
40	*Path offset*	0.3490	0.0876	0.2369	0.0886
50		1.6262	0.1573	0.1337	0.0798
60		7.2088	0.6390	0.2255	0.0903
70		11.5026	2.5197	0.3359	0.1243
80		11.2771	14.5141	0.4068	0.1928
90		8.7765	47.7082	0.6448	0.2515
100		6.5876	23.3846	1.8474	0.4185
110		5.2489	13.8823	5.8690	0.7233
40	$v_{x,final}$	38.4545	38.4527	38.4545	37.0048
50		47.4048	47.4019	33.4232	34.4253
60		55.4162	55.5527	33.4700	34.7615
70		-	61.3721	33.4887	34.4726
80		-	59.7524	33.2067	34.5730
90		-	48.8318	33.2135	34.5286
100		-	-	33.2185	34.6176
110		-	-	-	34.6503
40	*Fail*	0	0	0	0
50		US	0	0	0
60		US	0	0	0
70		US + RO	US + RO	0	0
80		US + RO	US + RO	0	0
90		US + RO	US + RO	RO	0
100		US	US + RO	US + RO	0
110		US	US + RO	US + RO	RO

Table 6.4: Performance table for simulation on dry asphalt, μ=0.9

v_{x0}	**Criteria**	**Open loop**	**Feedback**	**Feedforward**	**FB & FF**
40	$\dot{\psi}_{max}$	0.1258	0.1257	0.1258	0.1190
50		0.1594	0.1588	0.1479	0.1250
60		0.1959	0.1929	0.1584	0.1315
70		0.2460	0.2284	0.1661	0.1477
80		1.3388	0.2651	0.1712	0.1691
90		1.5901	0.3028	0.1781	0.1803
100		1.7716	1.4431	0.1776	0.1821
110		1.9081	1.6901	0.2055	0.1719
40	$a_{y,max}$	1.3939	1.3930	1.3939	1.2583
50		2.2037	2.1947	1.9490	1.3782
60		3.2420	3.1910	2.2569	1.5590
70		4.6976	4.3741	2.5600	1.9635
80		6.2448	5.6296	3.2266	2.5213
90		5.2031	6.1625	3.7716	2.8800
100		4.5840	6.1414	4.1673	3.2978
110		4.0237	5.0763	4.7529	3.8226
40	*Path offset*	0.1778	0.0971	0.1236	0.0951
50		1.3992	0.1193	0.1891	0.0704
60		2.5383	0.3348	0.3144	0.0898
70		17.4966	1.0619	0.4487	0.0997
80		11.5326	3.5160	0.6406	0.1458
90		10.0963	13.4359	0.8356	0.1958
100		7.1292	15.4199	1.1486	0.2766
110		4.9763	9.8519	1.2708	0.4414
40	$v_{x,final}$	38.4574	38.4566	38.4574	36.5342
50		47.4325	47.4293	33.7234	38.2594
60		55.6942	55.7366	33.7709	34.7749
70		61.8836	62.5010	33.7994	34.8445
80		-	66.2510	34.1310	34.9258
90		-	64.5401	33.5033	34.9333
100		-	-	33.4785	35.5165
110		-	-	33.4666	35.4507
40	*Fail*	0	0	0	0
50		US	0	0	0
60		US	0	0	0
70		US + RO	RO	0	0
80		US + RO	US + RO	0	0
90		US + RO	US + RO	RO	0
100		US + RO	US + RO	RO	0
110		US + RO	US + RO	US + RO	RO

7
Conclusion

Simulation results suggest that there is a potential for implementing a motion prediction control system to avoid understeer and rollover of a rigid truck. The implementation of a yaw controller alone enables the vehicle to remain tire traction for higher velocities, and as the yaw controller does not need any information of the road friction μ it is robust for variations in road friction. The controller does not, however, enforce any deceleration and in situations where the driver attempts a steering manoeuvre at an exceedingly high velocity the yaw controller independently may not be able to keep the necessary tire traction. The prediction algorithm is in simulation able to avoid understeer and rollover at further higher velocities by implementing a deceleration of the vehicle. A lowering of the velocity enables most driver steering manoeuvre to be carried out without reaching any critical limits and thus ensures that the truck remains stable. However simulations clearly suggest that the combination of both yaw control and prediction control is, for all road friction levels, the most successful. Results also show that the vehicle does not need to decelerate as much in order to maintain stability when a combination of prediction and yaw controller is enabled.

The prediction controller tested in simulation in this thesis is very strict, and although it successfully maintains stable conditions for significantly higher velocities at all variations of road friction, it may be unnecessarily conservative. For certain steering manoeuvres an online prediction controller may never be able to completely maintain stable conditions, such as if the vehicle enters a patch of ice at a high velocity, or in a sudden avoidance situation caused by another object on the road. In order to avoid such situations completely, the driver would have to always drive carefully at a low and safe velocity, which is not entirely realistic. However, the aim of this thesis is to investigate the possibility of implementing a motion prediction control in order to avoid understeer and rollover during normal driving conditions. Therefore, a further investigation of how strict the prediction controller needs to be will have to be carried out. A further idea may be to include an online assessment of the strictness based on the steering input from the driver. If the steering input is very sudden, the prediction controller may be more strict, however if the steering input is less sudden and suggests a normal turning action, the prediction control may be less strict. Especially in sudden steering situations, such as an avoidance situation, it may be necessary to initiate breaking immediately and a controller would be able to act quicker than a human, with limited reaction time, would.

The motion prediction control system derived in this thesis assumes that the road

friction μ is known during prediction. There is currently research being done at Volvo for online estimation of the road friction during driving, however we cannot assume this estimation will be accurate. It is therefore necessary to further investigate how well the prediction controller is able to maintain safe driving conditions with an uncertainty of the road friction estimations. Simulations may be run with and inaccurate estimate of μ, as well as with a road friction that varies during the simulation, to mimic a road with, for example, sudden ice patches. The results from this would have to be taken into account when assessing and tuning how strict the prediction controller should be.

7.1 Future Work

Although the simulation results from the motion prediction control system shows promise, there are still a lot of improvements needed before this controller could be implemented into a real truck. Primarily, the controller needs to be further assessed and tuned to a satisfactory level of strictness. Several things should be considered during this assessment, such as uncertainties in sensor inputs and estimations of road friction. There may also be uncertainties in the tire parameters, and experimental data show that most significantly the tire stiffness changes with tire wear. Lastly it must be considered that the prediction controller may be necessarily more strict for rapid steering inputs, which would suggest more critical situations. As the prediction control does not take into consideration other objects on the road, a rapid steering input is the only indication of an avoidance situation, and this might be factored into the consequent deceleration action.

A planned next step for the prediction control system is to implement parallel computation, which takes uncertainties into consideration. Parallel predictions would be run for the filtered input, as well as at the limits of uncertainties. These parallel predictions may give the worst case scenario inputs, which may improve final results. Including parallel predictions which compensates for uncertainties may also allow for the controller to be less unnecessarily strict, as safety scale factors could then be reduced.

Another very important next step is to maintain a low computation time. The aim for the safe operating envelope is to be able to implement it in real time. In order for this to be realisable, the predictions need to run in less time than the sampling time, which is 10 ms. Some functions may be run in parallel, however if the overall computation cannot be kept within 10 ms, then the prediction algorithm may need to be adjusted. The motion prediction system presented in this thesis has a computation time of approximately 7 ms, thus the system is currently realisable in real-time implementation.

Bibliography

[1] Mehdi Ahmadian. Integrating electromechanical systems in commercial vehicles for improved handling, stability, and comfort. *SAE International Journal of Commercial Vehicles*, 7(2):535–587, 2014.

[2] Anas Alrejjal and Khaled Ksaibati. Impact of crosswinds and truck weight on rollover propensity when negotiating combined curves. *International Journal of Transportation Science and Technology*, 2022.

[3] Gerardo Amato and Riccardo Marino. Reconfigurable slip vectoring control in four in-wheel drive electric vehicles. *Actuators*, 10(7), 2021.

[4] M. Bahaghighat, Sogol Kharrazi, Mathias Lidberg, Paolo Falcone, and B. Schofield. Predictive yaw and lateral control in long heavy vehicles combinations. pages 6403 – 6408, 12 2010.

[5] Mansour Keshavarz Bahaghighat. Yaw and lateral predictive control in long combinations of heavy vehicles. Master's thesis, Chalmers University of Technology, Sweden, 2011.

[6] Craig Borghesani, Yossi Chait, and Oded Yaniv. The qft frequency domain control design toolbox. Terasoft, Inc., 2003.

[7] V. Croulard, E. Godoy, and J. Boichot. Qft controller optimization for automatic design. In *Proceedings of the 39th IEEE Conference on Decision and Control (Cat. No.00CH37187)*, volume 5, pages 4735–4740 vol.5, 2000.

[8] M. daSilva, Gregory J. Ayres, and W. Najm. Crash problem definition and safety benefits methodology for stability control for single-unit medium and heavy trucks and large-platform buses. In *United States. Department of Transportation. National Highway Traffic Safety Administration*, 2009.

[9] EuroTest Quality Safety Mobility, Rue de la Science 41, 1040 Brussels - Belgium. *Road Works 2007 Guidelines in Europe*, 2007 [Online].

[10] Neal Gallagher. Savitzky-golay smoothing and differentiation filter. 01 2020.

[11] Torkel Glad and Lennart Ljung. *Control theory : multivariable and nonlinear methods.* Taylor & Francis, 2000.

[12] Eunhyek Joa, Kyongsu Yi, Kimo Sohn, and Hyungjune Bae. Four-wheel independent brake control to limit tire slip under unknown road conditions. *Control Engineering Practice*, 76:79–95, 2018.

[13] Sogol Kharrazi. *Steering based lateral performance control of long heavy vehicle combinations.* Doktorsavhandlingar vid Chalmers tekniska högskola. Ny serie: 3405. Chalmers University of Technology, 2012.

[14] Moad Kissai, Bruno Monsuez, Adriana Tapus, Xavier Mouton, and Didier Martinez. Optimal Yaw Rate Control for Over-Actuated Vehicles. In *WCX SAE World Congress Experience*, Detroit, United States, April 2020.

[15] E. Kuiper and J. J. M. Van Oosten. The pac2002 advanced handling tire model. *Vehicle System Dynamics*, 45(sup1):153–167, 2007.

[16] Leo Laine. *Reconfigurable motion control systems for over-actuated road vehicles.* Doktorsavhandlingar vid Chalmers tekniska högskola. Ny serie: 2641. Department of applied mechanics, Chalmers University of Technology, 2007.

[17] Stéphanie Lefèvre, Dizan Vasques, and Christian Laugier. A survey on motion prediction and risk assessment for intelligent vehicles. *ROBOMECH Journal*, 2014.

[18] Michael Robertson Levén, Anders Sjöblom, Mathias Lidberg, and Brad Schofield. Derivation of linear single-track truck-dolly-semitrailer model with steerable axles. 2011.

[19] Peter Nilsson. *Traffic situation management for driving automation of articulated heavy road transports : from driver behaviour towards highway autopilot.* Doktorsavhandlingar vid Chalmers tekniska högskola. Ny serie: 4311. Chalmers University of Technology, 2017.

[20] Peter Nilsson and Kristoffer Tagesson. Single-track models of an a-double heavy vehicle combination. 2014.

[21] Hans B. Pacejka. *Tire and Vehicle Dynamics, Third Edition.* Butterworth Heinemann, 4 2012.

[22] Shahrokh Paravarzar and Belqes Mohammad. Motion prediction on self-driving cars: A review. *CoRR*, abs/2011.03635, 2020.

[23] Abraham Savitzky and M. J. E Golay. Smoothing and differentiation of data by simplified least squares procedures. *Analytical Chemistry*, 36:1627–1639, 1964.

[24] Annika Stensson Trigell, Malte Rothhämel, Joop Pauwelussen, and Karel Kural. Advanced vehicle dynamics of heavy trucks with the perspective of road safety. *Vehicle System Dynamics*, 55(10):1572–1617, 2017.

[25] Anders Wikström. Yaw rate and lateral acceleration sensor plausibilisation in an active front steering vehicle. 01 2007.

A

4x2 Tractor Semitrailer Model

A.0.1 Newton Model

The method for deriving a vehicle model for a two unit vehicle with the Newton method is done in the same way as for a single unit vehicle, as in Section 3.1. Figures A.1 and A.2 shows a vector representation of the spacial and dynamic parameters of the 4x2 tractor semitrailer combination.

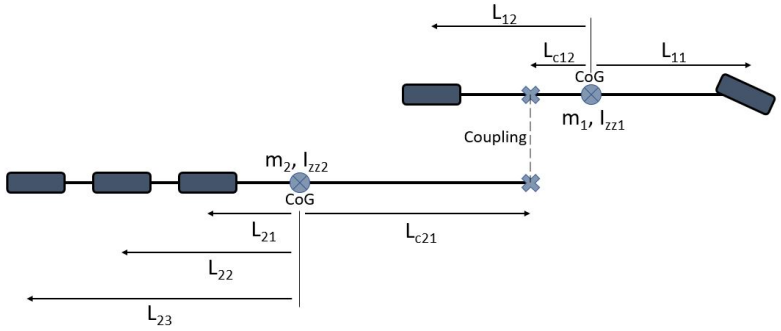

Figure A.1: Spacial parameters in a bicycle model of a two unit combination vehicle.

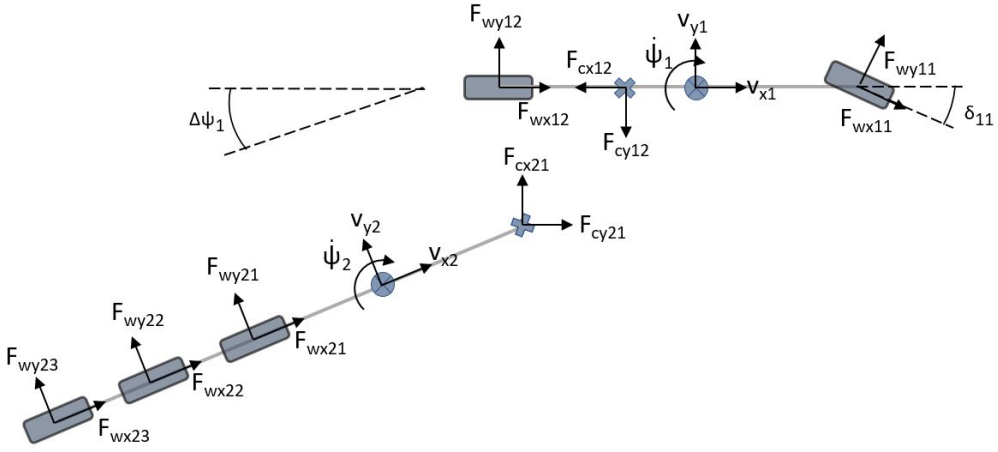

Figure A.2: Dynamic parameters in a bicycle model of a two unit combination vehicle.

The equations of motion for the tractor unit are as follows.

$$\begin{aligned} m_1(\dot{v}_{x1} - \dot{\psi}_1 v_{y1}) =& F_{wx11}\cos\delta_{11} - F_{wy11}\sin\delta_{11} + F_{wx12}\cos\delta_{12} - F_{wy12}\sin\delta_{12} \\ &+ F_{wx13} + F_{ecx12}\cos\psi_1 + F_{ecy12}\sin\psi_1 \\ m_1(\dot{v}_{y1} + \dot{\psi}_1 v_{x1}) =& F_{wx11}\sin\delta_{11} + F_{wy11}\cos\delta_{11} + F_{wx12}\sin\delta_{12} + F_{wy12}\cos\delta_{12} \\ &+ F_{wy13} - F_{ecx12}\sin\psi_1 + F_{ecy12}\cos\psi_1 \\ I_{zz1}\ddot{\psi}_1 =& (F_{wx11}\sin\delta_{11} + F_{wy11}\cos\delta_{11})L_{11} - (F_{wx12}\sin\delta_{12} + F_{wy12}\cos\delta_{12})L_{12} \\ &- F_{wy13}L_{13} - (-F_{ecx12}\sin\psi_1 + F_{ecy12}\cos\psi_1)L_{c12} \end{aligned} \tag{A.1}$$

The equations of motion for the semitrailer unit are as follows.

$$\begin{aligned} m_2(\dot{v}_{x2} - \dot{\psi}_2 v_{y2}) &= F_{wx21} + F_{wx22} + F_{wx23} + F_{ecx21}\cos\psi_2 + F_{ecy21}\sin\psi_2 \\ m_2(\dot{v}_{y2} - \dot{\psi}_2 v_{x2}) &= F_{wy21} + F_{wy22} + F_{wy23} - F_{ecx21}\sin\psi_2 + F_{ecy21}\cos\psi_2 \\ I_{zz2}\ddot{\psi}_2 &= -F_{wy21}L_{21} - F_{wy22}L_{22} - F_{wy23}L_{23} + (-F_{ecx21}\sin\psi_2 + F_{ecy21}\sin\psi_2)L_{c21} \end{aligned} \tag{A.2}$$

Articulation angle rate is described as

$$\Delta\dot{\psi}_1 = \dot{\psi}_1 - \dot{\psi}_2 \tag{A.3}$$

Newton's third law of motion is applied to the coupling forces between units, such that

$$\begin{aligned} F_{ecx12} &= -F_{ecx21} \\ F_{ecy12} &= -F_{ecy21} \\ \text{General form:} & \\ \mathbf{F}_{ec,n,p+1} &= -\mathbf{F}_{c,n+1,p} \end{aligned} \tag{A.4}$$

Assuming a linear lateral tyre model we get

$$\begin{aligned} F_{wynm} &= -CC_{ynm} \cdot F_{znm} \cdot S_{ynm} \\ S_{ynm} &= \frac{v_{wynm}}{|v_{wxnm}|} \\ C_{ynm} &= CC_{ynm} \cdot F_{znm} \end{aligned} \tag{A.5}$$

where

$$\mathbf{v}_{wnm} = \mathbf{R}(\delta_{nm}) \cdot (\mathbf{v}_n + \dot{\Psi}_n \times \mathbf{r}_{nm}) \tag{A.6}$$

C_{ynm} is the cornering stiffness [N/rad] and CC_{ynm} is the cornering coefficient [1/rad], where the cornering stiffness is normalised with vertical load. S_{ynm} denotes the tyre lateral slip.

There is a constraint on unit velocities.

$$\mathbf{v}_2 + \dot{\Psi}_2 \times \mathbf{r}_{c2} = R(\Delta\psi_n) \cdot (\mathbf{v}_1 + \dot{\Psi}_1 \times \mathbf{r}_{c1}) \tag{A.7}$$

Cross product gives the centrifugal force from turning, which gives rise to an addition to the lateral force. The rotation matrix is from unit 1 frame to unit 2 frame.

Kinematic equations linking the towing unit to the trailing unit, for velocity.

$$\mathbf{v}_{n+1} = R(\Delta\psi_n) \cdot (\mathbf{v}_n + \dot{\Psi}_n \times \mathbf{r}_{cnp}) - \dot{\Psi}_{n+1} \times \mathbf{r}_{c(n+1)p} \tag{A.8}$$

This gives the constraints for the coupling force.

$$\begin{aligned} v_{x2} &= v_{x1} \cos\Delta\psi_1 - (v_{y1} - \dot{\psi}_1 L_{c12}) \sin\Delta\psi_1 \\ v_{y2} &= v_{x1} \sin\Delta\psi_1 + (v_{y1} - \dot{\psi}_1 L_{c12}) \cos\Delta\psi_1 - \dot{\psi}_2 L_{c21} \end{aligned} \tag{A.9}$$

Note that these equations above hold for norm L_{c12}, and does not hold if L_{c12} is considered as negative.

Lateral acceleration of a unit i, where j denotes the axle.

$$\Gamma_{yi} = \sum F_{vyij} + F_{vicy} \tag{A.10}$$

Lateral acceleration of front or rear of a unit.

$$\Gamma_{y,f/r} = \Gamma_y + \psi_1^2 * l_{cog-f/r} \tag{A.11}$$

Note that the length to the front is denoted as positive, and the length to the rear is denoted as negative.

A.0.2 Lagrange Model

Due to issues with the coupling forces when deriving a model using the Newton formalism, another model using the Lagrange formalism was also derived. This model is based on the Euler-Lagrange equations [19], [13], [20], [18] (2^{nd} kind Lagrange equations), which are defined as:

$$\frac{d}{dt}(\frac{\partial L}{\partial \dot{q}_i}) = \frac{\partial L}{\partial q_i} \tag{A.12}$$

L is the smooth Lagrangian function, defined as the difference between the kinetic energy T and the potential energy V, and q_i is a vector of the generalised coordinates, describing a point in the configuration space.

$$\frac{d}{dt}(\frac{\partial T}{\partial \dot{q}_i} - \frac{\partial T}{\partial \dot{q}_i} + \frac{\partial v}{\partial q_i}) = Q_i \tag{A.13}$$

Q_i is the generalised forces, q_i is the generalised coordinates. For tractor semitrailer combination the generalised coordinates are defined as

$$q = \begin{bmatrix} X & Y & \psi_1 & \Delta\psi \end{bmatrix} \tag{A.14}$$

X and Y are the global coordinates of the first unit.

Velocities first unit are written as

$$\begin{bmatrix} v_x \\ v_y \end{bmatrix} = \begin{bmatrix} \cos\psi_1 & \sin\psi_1 \\ -\sin\psi_1 & \cos\psi_1 \end{bmatrix} \begin{bmatrix} \dot{X} \\ \dot{Y} \end{bmatrix} \tag{A.15}$$

We define T_1 and T_2 as non-linear functions of the quasi coordinates.

$$T_1 = T_1(v_{x1}, v_{y1}, \dot{\psi}_1) \tag{A.16}$$

$$T_2 = T_2(v_{x1},\ v_{y1},\ \dot{\psi}_1,\ \Delta\psi,\ \Delta\dot{\psi} \tag{A.17}$$

$$\frac{\partial T}{\partial \dot{X}} = \frac{\partial T}{\partial v_{x1}}\frac{\partial v_{x1}}{\partial \dot{X}} + \frac{\partial T}{\partial v_{y1}}\frac{\partial v_{y1}}{\partial \dot{X}} = A\,\cos\psi_1 - B\,\sin\psi_1 \tag{A.18}$$

$$\frac{\partial T}{\partial \dot{Y}} = \frac{\partial T}{\partial v_{x1}}\frac{\partial v_{x1}}{\partial \dot{Y}} + \frac{\partial T}{\partial v_{y1}}\frac{\partial v_{y1}}{\partial \dot{Y}} = A\,\sin\psi_1 - B\,\cos\psi_1 \tag{A.19}$$

where

$$A = \frac{\partial T}{\partial v_{x1}} \quad \text{and} \quad B = \frac{\partial T}{\partial v_{y1}} \tag{A.20}$$

$$\frac{\partial T}{\partial \psi} = \frac{\partial T}{\partial v_{x1}} v_{y1} - \frac{\partial T}{\partial v_{y1}} v_{x1} \tag{A.21}$$

Now considering our semitrailer vehicle. The kinetic energy is defined as the sum of rotational and translational energy for all units.

$$T = \sum_{i=1}^{2} \frac{1}{2} m_i\, \bar{v}_i^2 + \frac{1}{2} I_{zz,i} \dot{\psi}_i^2 \tag{A.22}$$

m_i are the masses and $I_{zz,i}$ are the moments of inertia around the z-axis. The potential energy for system is zero. v_i is the translational velocity and ψ_i is the rotational velocity.

Global position vectors:

$$\begin{aligned} \bar{p}_1 &= \begin{bmatrix} X & Y \end{bmatrix} \\ \bar{p}_2 &= \begin{bmatrix} X - L_{c12}\cos\psi_1 - L_{21}\cos\psi_2 \\ Y - L_{c12}\sin\psi_1 - L_{21}\sin\psi_2 \end{bmatrix}^T \end{aligned} \tag{A.23}$$

$$\begin{aligned} \bar{v}_1 &= \frac{d}{dt}\bar{p}_1 = \begin{bmatrix} \dot{X} & \dot{Y} \end{bmatrix} \\ \bar{v}_2 &= \frac{d}{dt}\bar{p}_2 = \begin{bmatrix} \dot{X} + L_{c12}\dot{\psi}_1 \sin\psi_1 + L_{21}\dot{\psi}_2 \sin\psi_2 \\ \dot{Y} - L_{c12}\dot{\psi}_1 \cos\psi_1 - L_{21}\dot{\psi}_2 \cos\psi_2 \end{bmatrix}^T \end{aligned} \tag{A.24}$$

which gives kinetic energy:

$$\begin{aligned} T =& \frac{1}{2}[I_{zz,1}\dot{\psi}_1^2 + I_{zz,2}\dot{\psi}_2^2 + m_1(\dot{v}_{x1}^2 + \dot{v}_{y1}^2) \\ &+ m_2((\dot{v}_{x1} + L_{c12}\dot{\psi}_1 \sin\psi_1 + L_{21}\dot{\psi}_2 \sin\psi_2)^2 + (\dot{v}_{y1} - L_{c12}\dot{\psi}_1 \cos\psi_1 - L_{21}\dot{\psi}_2 \cos\psi_2)^2)] \end{aligned} \tag{A.25}$$

Generalised forces defined as:

$$Q_i = \sum_{k=1}^{3} F_k \frac{\partial p_k}{\partial q_i} \tag{A.26}$$

$k = \{1, 2, 3\}$ is the axle positions, where the three rear tires of the second unit are contracted into one for simplicity. $i = \{1, 2, 3, 4\}$ are the generalised coordinates.

Tire forces in global frame:

$$\begin{aligned} F_{1f} &= \begin{bmatrix} F_{x1f}\cos(\psi_1+\delta) - F_{y1f}\sin(\psi_1+\delta) \\ F_{x1f}\sin(\psi_1+\delta) + F_{y1f}\cos(\psi_1+\delta) \end{bmatrix} \\ F_{1r} &= \begin{bmatrix} F_{x1r}\cos\psi_1 - F_{y1r}\sin\psi_1 \\ F_{x1r}\sin\psi_1 + F_{y1r}\cos\psi_1 \end{bmatrix} \\ F_{2r} &= \begin{bmatrix} F_{x2r}\cos\psi_2 - F_{y2r}\sin\psi_2 \\ F_{x2r}\sin\psi_2 + F_{y2r}\cos\psi_2 \end{bmatrix} \end{aligned} \tag{A.27}$$

Tire positions in global frame:

$$\begin{aligned} p_{1f} &= \begin{bmatrix} X + L_{11}\cos\psi_1 \\ Y + L_{11}\sin\psi_1 \end{bmatrix} \\ p_{1r} &= \begin{bmatrix} X - L_{12}\cos\psi_1 \\ Y - L_{12}\sin\psi_1 \end{bmatrix} \\ p_{2r} &= \begin{bmatrix} X - L_{c12}\cos\psi_1 - (L_{c21}+L_{2r})\cos(\psi_1+\Delta\psi) \\ Y - L_{c12}\sin\psi_1 - (L_{c21}+L_{2r})\sin(\psi_1+\Delta\psi) \end{bmatrix} \end{aligned} \tag{A.28}$$

Transformation to quasi-coordinates:

$$\begin{bmatrix} Q_x \\ Q_y \end{bmatrix} = \begin{bmatrix} \cos\psi_1 & \sin\psi_1 \\ -\sin\psi_1 & \cos\psi_1 \end{bmatrix} \begin{bmatrix} Q_X \\ Q_Y \end{bmatrix} \tag{A.29}$$

$$\begin{aligned} Q_X =& F_{x1r}\cos\psi_1 + F_{x1f}\cos(\psi_1+\delta) + F_{x2r}\cos(\psi_1+\delta) - F_{y1r}\sin\psi_1 \\ & - F_{y1f}\sin(\psi_1+\delta - F_{y2r}\sin\psi_1 + \Delta\psi \\ Q_Y =& F_{x1r}\sin\psi_1 + F_{x1f}\sin(\psi_1+\delta) + F_{x2r}\sin(\psi_1+\delta) + F_{y1r}\cos\psi_1 \\ & + F_{y1f}\cos(\psi_1+\delta + F_{y2r}\cos\psi_1 + \Delta\psi \\ Q_{\psi_1} =& - L_{12}F_{y1r} - (L_{c21}+L_{2r})F_{y2r} - L_{c12}F_{y2r}\cos\Delta\psi \\ & + L_{11}(F_{y1f}\cos\delta + F_{x1f}\sin\delta) + F_{x2r}\sin\Delta\psi \\ Q_{\Delta\psi} =& - (L_{c21}+L_{2r})F_{y2r} \end{aligned} \tag{A.30}$$

B

Tire Models

B.1 Full Pacejka 2002 Model

The modified PAC2002 model presented in Section 4.1.3 is a simplified adaption of the full PAC2002 model described in this section. The PAC2002 model is a tire model which describes the tire forces F_x and F_y as a combination of a pure slip function and a combined slip weighting function.

$$F_x = F_{x0}\, G_{x\alpha}(\alpha,\, \kappa,\, F_z) \tag{B.1}$$
$$F_y = F_{y0}\, G_{y\kappa}(\alpha,\, \kappa,\, \gamma,\, F_z) + S_{Vy\kappa} \tag{B.2}$$

The normalised vertical load and road slip quantities are computed.

$$\begin{aligned} df_z &= \frac{F_z - F_{z0}}{F_{z0}} \\ \mu_x &= (p_{Dx1} + p_{Dx2}\, df_z)\,(1 - p_{Dx3}\, \gamma_x^2)\, \lambda_{\mu x} \\ \mu_y &= (p_{Dy1} + p_{Dy2}\, df_z)\,(1 - p_{Dy3}\, \gamma_y^2)\, \lambda_{\mu y} \end{aligned} \tag{B.3}$$

where λ_μ is the road friction.

Longitudinal force at pure slip is calculated using the magic formula.

$$F_{x_0} = D_x\, \sin(C_x\, \arctan(B_x\, \kappa_x - E_x\, (B_x\, \kappa_x - \arctan(B_x\, \kappa_x)))) + S_{Vx} \tag{B.4}$$

$$\kappa_x = \kappa + S_{Hx} \tag{B.5}$$
$$\gamma_x = \gamma\, \lambda_{\gamma x} \tag{B.6}$$

The coefficients to the magic formula are calculated, where S_{Hx} and S_{Vx} are shift factors.

$$\begin{aligned} C_x &= p_{Cx1}\, \lambda_{C_x} \\ D_x &= \mu_x\, F_z\, \zeta_1 \\ E_x &= (p_{Ex1} + p_{Ex2}\, df_z + p_{Ex3}\, df_z^2)\,(1 - p_{Ex4}\, sign(\kappa_x))\, \lambda_{Ex} \\ K_x &= F_z\, (p_{Kx1} + p_{Kx2}\, df_z)\, exp(p_{Kx3}\, df_z)\, \lambda_{Kx} \\ &\quad (K_x = B_x\, C_x\, D_x \quad \text{Longitudinal stiffness}) \\ B_x &= \frac{K_x}{C_x\, D_x} \\ S_{Hx} &= (p_{Hx1} + p_{Hx2}\, df_z)\, \lambda_{Hx} \\ S_{Vx} &= F_z\, (p_{Vx1} + p_{Vx2}\, df_z)\, \lambda_{Vx}\, \lambda_{\mu x}\, \zeta_1 \end{aligned} \tag{B.7}$$

Coefficient	Description
p_{Cx1}	Longitudinal force shape factor
p_{Dx1}	Longitudinal friction μ_x at $F_{z,nom}$
p_{Dx2}	Variation of friction μ_x with load
p_{Dx3}	Variation of friction μ_x with inclination
p_{Ex1}	Longitudinal curvature at $F_{z,nom}$
p_{Ex2}	Variation of curvature with load
p_{Ex3}	Variation of curvature with load squared
p_{Ex4}	Factor in curvature while driving
p_{Kx1}	Longitudinal slip stiffness at $F_{z,nom}$
p_{Kx2}	Variation of slip stiffness with load
p_{Kx3}	Exponent in slip stiffness with load
p_{Hx1}	Horizontal shift at $F_{z,nom}$
p_{Hx2}	Variation of shift with load
p_{Vx1}	Vertical shift at $F_{z,nom}$
p_{Vx2}	Variation of shift with load

Table B.1: Description of the longitudinal pure slip tire force coefficients.

The longitudinal tire force for combined slip is calculated as

$$F_x = D_{x\alpha}\,\cos(C_{x\alpha}\,\arctan(B_{x\alpha} - E_{x\alpha}\,(B_{x\alpha}\,\alpha_s - \arctan(B_{x\alpha}\,\alpha_s)))) \tag{B.8}$$

$$\alpha_s = \alpha + S_{Hx\alpha} \tag{B.9}$$

with coefficients calculated as

$$\begin{aligned} C_{x\alpha} &= r_{Cx1} \\ B_{x\alpha} &= r_{Bx1}\,\cos(\arctan(r_{Bx2}\kappa))\,\lambda_{x\alpha} \\ D_{x\alpha} &= \frac{F_x 0}{\cos(C_{x\alpha}\,\arctan(B_{x\alpha}\,S_{Hx\alpha} - E_{x\alpha}\,(B_{x\alpha}\,S_{Hx\alpha} - \arctan(B_{x\alpha}\,S_{Hx\alpha}))))} \\ E_{x\alpha} &= r_{Ex1} + r_{Ex2}\,df_z \\ S_{Hx\alpha} &= r_{Hx1} \end{aligned} \tag{B.10}$$

The longitudinal weighting function is calculated as

$$G_{x\alpha} = \frac{\cos(C_{x\alpha}\,\arctan(B_{x\alpha}\,\alpha_s - E_{x\alpha}\,(B_{x\alpha}\,\alpha_s - \arctan(B_{x\alpha}\,\alpha_s))))}{\cos(C_{x\alpha}\,\arctan(B_{x\alpha}\,S_{Hx\alpha} - E_{x\alpha}\,(B_{x\alpha}\,S_{Hx\alpha} - \arctan(B_{x\alpha}\,S_{Hx\alpha}))))} \tag{B.11}$$

Coefficient	Description
r_{Bx1}	Slope factor for combined slip longitudinal force reduction
r_{Bx2}	Variation of slope longitudinal force reduction with κ
r_{Cx1}	Shape factor for combined slip longitudinal force reduction
r_{Ex1}	Curvature factor of combined longitudinal force
r_{Ex2}	Curvature factor of combined longitudinal force with load
r_{Hx1}	Shift factor for combined slip longitudinal force reduction

Table B.2: Description of the longitudinal combined slip tire force coefficients.

Lateral force at pure slip is calculated using the magic formula.

$$F_{y0} = D_y \sin(C_y \arctan(B_y \alpha_y - E_y (B_y \alpha_y - \arctan(B_y \alpha_y)))) + S_{Vy} \tag{B.12}$$

$$\alpha_y = \alpha + S_{Hy} \tag{B.13}$$

$$\gamma_y = \gamma \lambda_{\gamma y} \tag{B.14}$$

The coefficients to the lateral force at pure slip formula are calculated as

$$\begin{aligned}
C_y &= p_{Cy1} \lambda_{Cy} \\
D_y &= \mu_y F_z \zeta_2 \\
E_y &= (p_{Ey1} + p_{Ey2} df_z)(1 - (p_{Ey3} + p_{Ey4} \gamma_y) \operatorname{sgn}(\alpha_y)) \lambda_{Ey} \\
K_{y0} &= p_{Ky1} F_{z_0} \sin(2 \arctan(\frac{F_z}{p_{Ky2} F_0 \lambda_{F_{z_0}}})) \lambda_{F_{z_0}} \lambda_{Ky} \\
K_y &= K_{y0} (1 - p_{Ky3} |\gamma_y|) \zeta_3 \\
B_y &= \frac{K_y}{C_y D_y} \\
S_{Hy} &= (p_{Hy1} + p_{Hy2} df_z) \lambda_{Hy} + p_{Hy3} \gamma_y \zeta_0 + \zeta_4 - 1 \\
S_{Vy} &= F_z ((p_{Vy1} + p_{Vy2} df_z) \lambda_{Vy} + (p_{Vy3} + p_{Vy4} df_z) \gamma_y) \lambda_{\mu y} \zeta_4 \\
K_{y\gamma 0} &= p_{Hy3} K_{y0} + F_z (p_{Vy3} + p_{Vy4} df_z)
\end{aligned} \tag{B.15}$$

Coefficient	Description
p_{Cy1}	Lateral force shape factor
p_{Dy1}	Lateral friction μ_y
p_{Dy2}	Variation of friction μ_y with load
p_{Dy3}	Variation of friction μ_y with squared inclination
p_{Ey1}	Lateral curvature at $F_{z,nom}$
p_{Ey2}	Variation of curvature with load
p_{Ey3}	Inclination dependency of curvature
p_{Ey4}	Variation of curvature with inclination
p_{Ky1}	Maximum lateral stiffness value
p_{Ky2}	Load at which maximum lateral stiffness is reached
p_{Ky3}	Variation of lateral stiffness with inclination
p_{Hy1}	Horizontal shift at $F_{z,nom}$
p_{Hy2}	Variation of shift with load
p_{Hy3}	Variation of shift with inclination
p_{Vy1}	Vertical shift at $F_{z,nom}$
p_{Vy2}	Variation of shift with load
p_{Vy3}	Variation of shift with inclination
p_{Vy4}	Variation of shift with inclination and load

Table B.3: Description of the lateral pure slip tire force coefficients.

The lateral tore force at combined slip is calculated as

$$F_y = D_{y\kappa} \cos(C_{y\kappa} \arctan(B_{y\kappa} \kappa_s - E_{y\kappa} (B_{y\kappa} \kappa_s - \arctan(B_{y\kappa} \kappa_s)))) + S_{Vy\kappa} \tag{B.16}$$

$$\kappa_s = \kappa + S_{H y\kappa} \tag{B.17}$$

with coefficients

$$\begin{aligned}
B_{y\kappa} &= r_{By1}\, \cos(\arctan(r_{By2}\,(\alpha - r_{By3})))\, \lambda_{y\kappa} \\
C_{y\kappa} &= r_{Cy1} \\
D_{y\kappa} &= \frac{F_{y0}}{\cos(C_{y\kappa}\, \arctan(B_{y\kappa}\, S_{H y\kappa} - E_{y\kappa}\,(B_{y\kappa}\, S_{H y\kappa} - \arctan(B_{y\kappa}\, S_{H y\kappa}))))} \\
E_{y\kappa} &= r_{Ey1} + r_{Ey2}\, df_z \\
S_{H y\kappa} &= r_{Hy1} + r_{Hy2}\, df_z \\
S_{V y\kappa} &= D_{V y\kappa}\, \sin(r_{Vy5}\, \arctan(r_{Vy6}\, \kappa))\, \lambda_{V y\kappa} \\
D_{V y\kappa} &= \mu_y\, F_z\, (r_{Vy1} + r_{Vy2}\, df_z + r_{Vy3}\, \gamma)\, \cos(\arctan(r_{Vy4}\, \alpha))
\end{aligned} \tag{B.18}$$

The lateral weighting function is calculated as

$$G_{y\kappa} = \frac{\cos(C_{y\kappa}\, \arctan(B_{y\kappa}\, \kappa_s - E_{y\kappa}\,(B_{y\kappa}\, \kappa_s - \arctan(B_{y\kappa}\, \kappa_s))))}{\cos(C_{y\kappa}\, \arctan(B_{y\kappa}\, S_{H y\kappa} - E_{y\kappa}\,(B_{y\kappa}\, S_{H y\kappa} - \arctan(B_{y\kappa}\, S_{H y\kappa}))))} \tag{B.19}$$

Coefficient	**Description**
r_{By1}	Slope factor for combined slip lateral force reduction
r_{By2}	Variation of slope lateral force reduction with α
r_{By3}	Shift term for α in slope lateral force reduction
r_{Cy1}	Shape factor for combined slip lateral force reduction
r_{Ey1}	Curvature factor of combined lateral force
r_{Ey2}	Curvature factor of combined lateral force with load
r_{Hy1}	Shift factor for combined slip lateral force reduction
r_{Hy2}	Shift factor for combined slip lateral force reduction with load
r_{Vy1}	κ-induced side force at $F_{z,nom}$
r_{Vy2}	Variation of κ-induced side force with load
r_{Vy3}	Variation of κ-induced side force with inclination
r_{Vy4}	Variation of κ-induced side force with α
r_{Vy5}	Variation of κ-induced side force with κ
r_{Vy6}	Variation of κ-induced side force with $\arctan(\kappa)$

Table B.4: Description of the lateral combined slip tire force coefficients.

B.2 Simplified Pacejka Tire Model

A simplification of the Pacejka magic formulas was made where the linear parts of the tire forces are matched, but which is reversible. This was done since we needed a reversible formula which kept the linear behaviour for the prediction model. A more sophisticated prediction model was later implemented and this simplified model was then discarded. This method calculates the linear pure slip tire force slope using the Pacejka tire model, and saturates the tire force at the peak value. This is then multiplied with a weighting function derived in this thesis from the Pacejka model

to account for combined slip.

The longitudinal pure slip tire force is calculated as

$$F_{x_0} = \min(K_x\,\kappa\,,\; D_x\,sign(\kappa)) \tag{B.20}$$

The lateral pure slip tire force is calculated as

$$F_{y_0} = \min(K_y\,\alpha\,,\; D_y\,sign(\alpha)) \tag{B.21}$$

The weighting functions are a regression model of the PAC2002 weighting functions and are calculated as

$$G_x = b_{x,1} + b_{x,2}\,|\kappa| + b_{x,3}\,|\alpha| + b_{x,4}\,\kappa^2 + b_{x,5}\,\alpha^2 \quad , \qquad G_x \in [-1, 1] \tag{B.22}$$

$$G_y = b_{y,1} + b_{y,2}\,|\kappa| + b_{y,3}\,|\alpha| + b_{y,4}\,\kappa^2 + b_{y,5}\,\alpha^2 \quad , \qquad G_y \in [-1, 1] \tag{B.23}$$

where

$$b_x = \begin{bmatrix} 0.9902 \\ 0.2323 \\ -2.7023 \\ 1.1533 \\ 3.4267 \end{bmatrix} \quad , \qquad b_y = \begin{bmatrix} 0.9166 \\ -2.0828 \\ 0.7175 \\ 0.6241 \\ -0.0442 \end{bmatrix} \tag{B.24}$$

The tire forces for combined slip are then calculated as

$$F_x = F_{x_0}\,G_x \tag{B.25}$$

$$F_y = F_{y_0}\,G_y \tag{B.26}$$

Figure B.1 shows a comparison of the simplified Pacejka model,the PAC2002 model and the Brush model, for varying values of κ, α and μ. We see that the simplified Pacejka model follows the PAC2002 model well. The Brush model is presented in Section B.3.

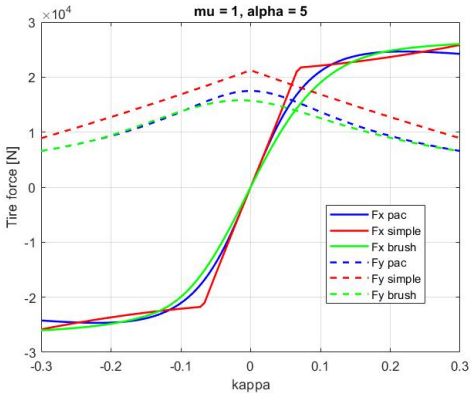

(a) Longitudinal tire force for μ=1, α=5 degrees.

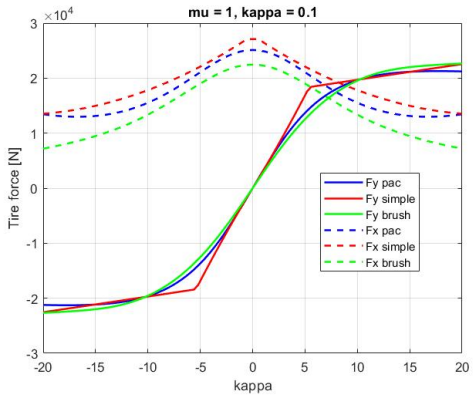

(b) Lateral tire force for μ=1, κ=0.1.

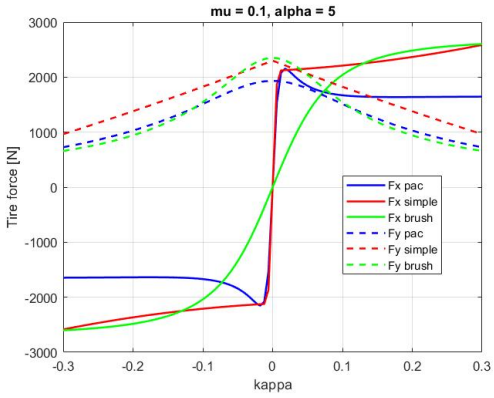

(c) Longitudinal tire force for μ=0.1, α=5 degrees.

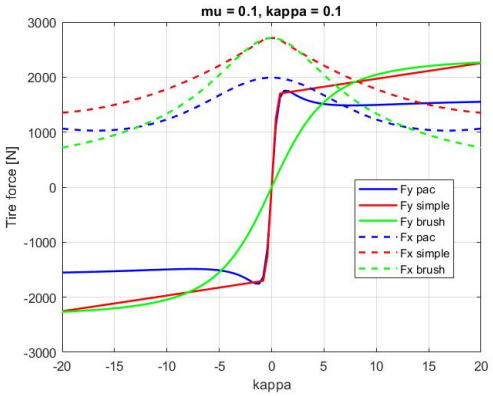

(d) Lateral tire force for μ=0.1, κ=0.1.

Figure B.1: Comparison between the PAC2002 model, the simplified Pacjeka model and the Brush model.

Figure B.2 shows a comparison between the PAC2002 weighting functions and the regression models derived in this thesis. It was found that the lateral weighting function G_y was negligibly dependent on load, however the longitudinal weighting function G_x was not. The regression of the lateral weighting function was initially used in the prediction model, however this entire simplified Pacejka model was later abandoned for the modified PAC2002 model.

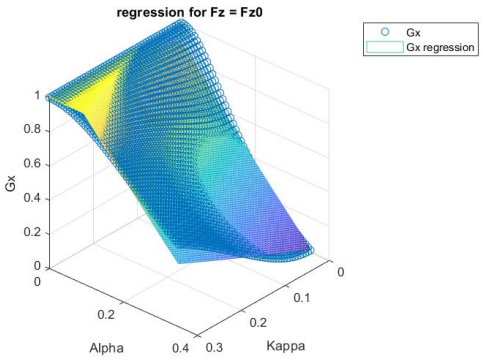

(a) G_x regression for normal load, $F_z = F_{z0}$.

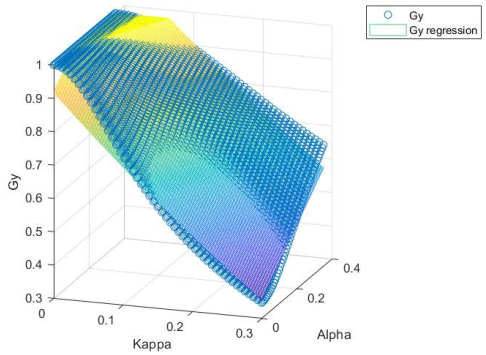

(b) G_y regression.

Figure B.2: Comparison between the PAC2002 weighting functions and the regression models.

B.3 Modified Brush Tire Model

The Brush model considers a row of elastic bristles that touch the road plane and can deflect in a direction parallel to the road surface. These bristles are referred to as tread elements, and their compliance is the elasticity of the combination of carcass, belt and actual tread elements of the real tire. The bristles are assumed to enter the contact zone to the road at a perpendicular angle to the road. At free rolling with no slip the tread elements are assumed to remain vertical and develop no deflections throughout the contact zone. Possible rolling resistance is neglected. Parabolic pressure distribution is assumed. This section provides a brief description to how tire forces are calculated using the modified Brush model, which is an adaption of the Brush model developed in this thesis.

The brush combined slip model, for mathematical simplicity, restricts itself to equal longitudinal and lateral stiffness of the tread elements.

$$c_p = c_{px} = c_{py} \tag{B.27}$$

We will however not apply this restriction, and instead follow the model for individual longitudinal and lateral stiffness.

The brush model considers equal and constant friction coefficients.

$$\mu = \mu_x = \mu_y \tag{B.28}$$

Time from the point of entrance to the point at distance x in front of contact centre is calculated.

$$\Delta t = \frac{a - x}{V_r} \tag{B.29}$$

Deflection of an element still in adhesion is, in vectorial form

$$\mathbf{e} = \begin{pmatrix} u \\ v \end{pmatrix} = -\boldsymbol{V}_s \Delta t = -\frac{\boldsymbol{V}_s}{V_r}(a - x) \tag{B.30}$$

Introducing alternative, theoretical, slip quantity, in vectorial form

$$\boldsymbol{\sigma} = \begin{pmatrix} \sigma_x \\ \sigma_y \end{pmatrix} = -\frac{\boldsymbol{V}_s}{V_r} = -\frac{1}{V_r}\begin{pmatrix} V_{sx} \\ V_{sy} \end{pmatrix} \tag{B.31}$$

with linear speed of rolling

$$V_r = V_x - V_{sx} \tag{B.32}$$

Relation between theoretical slip and practical slip quantities κ and α are calculated as

$$\boldsymbol{\sigma}_x = \frac{\kappa}{1+\kappa} \tag{B.33}$$

$$\boldsymbol{\sigma}_y = \frac{\tan\alpha}{1+\kappa} \tag{B.34}$$

Deflection then becomes

$$\boldsymbol{e} = (a-x)\boldsymbol{\sigma} \tag{B.35}$$

Thus longitudinal and lateral deflections are governed by σ_x and σ_y respectively, and are independent of each other, which would not be the case if expressed in terms of practical slip quantities κ and α.

Local horizontal contact force acting on the tips of the tread elements, per unit contact length in the adhesion region is caluclated as

$$\boldsymbol{q} = c_p(a-x)\boldsymbol{\sigma} \tag{B.36}$$

The sliding region is entered when

$$q = |\boldsymbol{q}| = \sqrt{q_x^2 + q_y^2} > \mu q_z \tag{B.37}$$

and the friction force vector then becomes, in the sliding region

$$\boldsymbol{q} = -\frac{\boldsymbol{V_s}}{V_s}\mu q_z = \frac{\boldsymbol{\sigma}}{\sigma}\mu q_z \tag{B.38}$$

where

$$V_s = \sqrt{V_{sx}^2 + V_{sy}^2} \tag{B.39}$$

and

$$\sigma = \sqrt{\sigma_x^2 + \sigma_y^2} \tag{B.40}$$

Similarly, the magnitude of deflection of an element becomes

$$e = |\boldsymbol{e}| = \sqrt{u^2 + v^2} \tag{B.41}$$

Point of transition from adhesion region to sliding region is obtained from

$$c_p e = \mu q_z \tag{B.42}$$

or

$$c_p\sigma(a - x_t) = \frac{3}{4}\mu F_z\frac{a^2 - x_t^2}{a^3} \tag{B.43}$$

which yields

$$x_t = \frac{4}{3}\frac{c_p a^3 \sigma}{\mu F_z} - a = a(2\theta\sigma - 1) \tag{B.44}$$

We have that $\lambda = 1 - \theta\sigma$, and for the isotropic model parameter θ

$$\theta = \theta_x = \theta_y = \frac{2}{3}\frac{c_p a^2}{\mu F_z} \tag{B.45}$$

The slip at which total sliding starts is calculated as

$$\sigma_{sl} = \frac{1}{\theta} \tag{B.46}$$

Magnitude of total force $F = |\boldsymbol{F}|$ is calculated as

$$F = \mu F_z(1 - \lambda^3) = \mu F_z(3\theta\sigma - 3(\theta\sigma)^2 + (\theta\sigma)^3) \qquad \text{for} \quad \sigma \leq \sigma_{sl} \tag{B.47}$$

$$F = \mu F_z \qquad \text{for} \quad \sigma \geq \sigma_{sl} \tag{B.48}$$

The force vector acts in a direction opposite to $\boldsymbol{V}_s$ or $-\sigma$, hence

$$\boldsymbol{F} = F\frac{\boldsymbol{\sigma}}{\sigma} \tag{B.49}$$

From this, components F_x and F_y may be obtained.

DEPARTMENT OF SOME SUBJECT OR TECHNOLOGY
CHALMERS UNIVERSITY OF TECHNOLOGY
Gothenburg, Sweden
www.chalmers.se

CHALMERS
UNIVERSITY OF TECHNOLOGY